Source mechanisms of deep long period earthquakes beneath the Klyuchevskoy volcanic group (Kamchatka, Russia) inferred from S-to-P amplitude ratios

Nataliya Galina, Nikolai Shapiro

Source Mechanisms of Deep Long Period Earthquakes beneath the Klyuchevskoy Volcanic Group (Kamchatka, Russia) inferred from S-to-P amplitude ratios

Nataliya A. Galina[a,b,*], Nikolai M. Shapiro[a,]

[a] *Institut des Sciences de la Terre, Université Grenoble Alpes, CNRS UMR 5375, 38400, Grenoble, France*
[b] *Schmidt Institute of Physics of the Earth, Russian Academy of Sciences, 123242, Moscow, Russia*

Abstract

We study the long-period earthquakes that occur at the crust-mantle boundary beneath the Klyuchevskoy volcano group in Kamchatka in order to reconstruct their source mechanisms. These earthquakes are observed at frequencies between 1 and 4 Hz and the phases of their seismograms are strongly affected by the high-pass filtering required to remove the microseismic noise. Therefore, we decided to use an inversion method based on amplitude ratios between S- and P-waves. Considering the uncertainties associated with this method and potentially leading to non-uniqueness of the inversion, we decided not to explore the full space of the source parameters but to test a set of "elementary" mechanisms corresponding to processes possibly occurring within magmatic systems of volcanoes and their surroundings. Also, after measuring the raw amplitudes of P- and S- waves we corrected them for the site amplification effects. Based on the results of the inversion, the

*Corresponding author
Email address: natalia.galina96@gmail.com (Nataliya A. Galina)

Preprint submitted to Journal of Volcanology and Geothermal Research January 22, 2024

generation of the DLP earthquakes beneath Klyuchevskoy by shear faulting (as would be the case in thermomechanical stresses associated with cooling of deep intrusions) can be reasonably excluded. The observed signal amplitudes can be better explained with source mechanisms containing strong volumetric or single force components. The former can be associated with the pressure perturbation withing magmatic reservoirs or conduits and the latter with the sudden acceleration of the magma movement. The ensemble of our observations is compatible with the configuration when the magma is stored in nearly horizontal sills near the crust-mantle boundary and penetrates into the crust through conduits dipping south-southwest, in agreement with previously reported connection of the deep magmatic reservoir with the Bezymanny and Tolbachik volcanoes.

Keywords: Long-period seismicity, volcano monitoring, source mechanism

---

1. Introduction.

Analysis of seismic signals recorded in the vicinity of volcanoes is one of the key elements of the volcano monitoring and one of the important sources of information about active processes occurring at depths in the volcano plumbing systems (e.g., Chouet, 2003; Sparks, 2003; Nishimura and Iguchi, 2011; Zobin, 2011; Chouet and Matoza, 2013; McNutt and Roman, 2015; Matoza and Roman, 2022; Thelen et al., 2022). Volcanic seismicity is often divided into two main classes. The first class of signals associated with volcanic activity is composed of volcano-tectonic (VT) earthquakes (e.g., Roman and Cashman, 2006). These nearly impulsive signals are characterized by a wide spectral range (up to 15–20 Hz) and clear arrivals of P- and S-waves. As

their name suggests, the origin of the VT earthquakes is beleived to be similar to regular tectonic earthquakes and is associated with the brittle failure faulting of crustal rocks in the vicinity of volcanoes.

The second class of seismo-volcanic phenomena is called long-period (LP) seismicity and regroups a large variety of signals ranging from relatively short LP earthquakes to long duration tremors. These signals have typical frequencies of a few Hz and their origin is often associated with pressure fluctuations within magmatic and hydrothermal fluids (e.g., Chouet, 1996). Thus, the LP seismicity is believed to be directly related to the processes of the magma motion and pressurisation and to be able to provide reliable precursors of volcanic eruptions (e.g., White et al., 1996; Chouet and Matoza, 2013; Shapiro et al., 2017a).

While most of the observed LP seismicity originate at very shallow depths (less than 3-5 km), a particularly important sub-class known as the deep long period (DLP) earthquakes occurs at depths ranging from the middle crust to the crust-mantle boundary (25–40 km). The DLPs are usually linked with the processes occurring within the magmatic fluids at such large depths and can reflect the activation of deep-seated parts of the magmatic systems prior to eruptions. One of the first times, the swarms of DLP events were recorded beneath Mount Pinatubo (White et al., 1996) who linked them with the magma uprising from depth. Later DLPs were reported at different regions such as Cascadia (Nichols et al., 2011), the Aleutian arc (Power et al., 2004), Japan (Hasegawa and Yamamoto, 1994; Nakamichi et al., 2003; Aso et al., 2013; Niu et al., 2017; Yukutake et al., 2019; Kurihara et al., 2019; Ikegaya and Yamamoto, 2021; Kurihara and Obara, 2021), Kamchatka (Shapiro et al.,

2017a), Eifel (Hensch et al., 2019), and Hawaii (Wech et al., 2020).

Despite these numerous studies, physical processes leading to generation of DLP earthquakes and their seismic mechanisms remain poorly understood. Several hypotheses have been suggested. As already mentioned, White et al. (1996) considered the DLP seismicity being the elastic manifestation of the injection of deep-seated basaltic fluids without, however, proposing any physical model. Aso and Tsai (2014) suggested that the DLP earthquakes can be caused by thermal stresses induced by cooling of deep magma bodies. The relationship between the possible focal mechanisms and stress orientations suggested in this work again remained only at a qualitative level. The DLP activity beneath Mauna Kea volcano in Hawaii has been also suggested to be related to magma bodies cooling by Wech et al. (2020). These authors however relate the generation of the DLP earthquakes not with thermal stresses but with the degassing caused by so called "secondary boiling", i.e., the exsolution of volatiles during the crystallization of cooling magma. Again, no quantitative model relating the degassing and the generation of seismic waves has been suggested.

Bursts of DLP earthquakes occurring beneath active volcanoes and preceding their eruptions (e.g., White et al., 1996; Shapiro et al., 2017a) are unlikely to be explained by the cooling of old intrusions and are rather expected to be associated with the supply of the fresh magma to the plumbing system. For such situation, the model of Melnik et al. (2020) considered a possible DLP generating mechanism via the rapid growth of gas bubbles in response to the slow decompression of magma over-saturated with volatiles (CO_2–H_2O rich). These authors show that this model is compatible with the known

composition of the basaltic magma emitted by the Klyuchevskoy volcano in Kamchatka (Russia) where a sustained DLP activity is observed (Shapiro et al., 2017a) and also can reasonably explain amplitudes and frequencies of the observed DLP signals.

Kinematic moment-tensor inversion of the DLP earthquakes (e.g., Nakamichi et al., 2003; Aso and Ide, 2014; Hensch et al., 2019; Ikegaya and Yamamoto, 2021) was carried out with fitting the amplitudes and waveforms of body waves and generally demonstrated a strong volumetric component in the seismic source, which would be in agreement with the generating process involving pressure variations in magma. However, the results of such source inversion are associated with strong uncertainties because of the combination of noisy data with poorly known wave propagation.

In this work, we study the kinematic source parameters of 29 DLP earthquakes beneath the Klyuchevskoy volcano group (KVG) in Kamchatka, Russia recorded by temporary stations of a recent seismic experiment (Shapiro et al., 2017b). We use the fit to the observed amplitude ratios between P- and S-waves in order to constrain the source mechanism. We consider possible mass advection effects and add to the moment tensor a possible single force component (Takei and Kumazawa, 1994). At the same time, instead of performing a full inversion in the parameter space that my be subject to a strong uncertainty, we rather proceed with testing a set of "plausible" hypotheses resulting in source mechanisms with a reduced number of parameters.

In the following sections, we start with describing the studied volcanic system and the used dataset. We then discuss different hypotheses about the source mechanism and corresponding descriptions in terms of kinematic

source parameters. The inversion method is then introduced and applied to the records of 29 selected DLP earthquakes.

2. Klyuchevskoy volcano group and its seismic activity.

The Klyuchevskoy volcano group (KVG) is one of the largest clusters of subduction volcanoes in the World. Its most active volcano, Klyuchevskoy has produced over the past 7,000 years on average 1 cubic meter of erupted rock every second (Fedotov et al., 2010). This eruption rate is much higher than that of most volcanoes associated with subduction. Besides Klyuchevskoy, the KVG contains 12 other large stratovolcanoes. Two of them, Bezymianny and Tolbachik, have been also very active in the past few decades.

This elevated volcanic activity is related to the unique tectonic setting of the KVG located at the corner between the Kuril-Kamchatka and Aleutian trenches. The enhanced supply of the melt from the mantle in this region is likely caused by the the around-slab-edge asthenospheric flow (Yogodzinski et al., 2001; Levin et al., 2002) and related crustal extension (Green et al., 2020; Koulakov et al., 2020). Additionally, the underwater volcanic mountain range that stretches down to Hawaii, is subducted beneath this corner and the KVG, which may result in the release of fluids from the thick, highly hydrated Hawaiian-Emperor crust (Dorendorf et al., 2000).

The KVG volcanoes present a broad spectrum of eruptive styles, ranging from steady Hawaiian-type eruptions of Tolbachik to the strongly explosive eruptions of Bezymianny. At the same time, recent studies based on seismic tomography (Ivanov et al., 2016; Koulakov et al., 2017), seismicity (Shapiro et al., 2017a; Journeau et al., 2022), and thermal remote sensing (Coppola

et al., 2021) suggest that the volcanoes of the group can be interconnected and fed through one extended trans-crustal volcanic system.

The sustained volcanic activity of the KVG results in nearly constantly occurring seismicity including long periods of seismo-volcanic tremors (Droznin et al., 2015; Soubestre et al., 2018, 2019; Journeau et al., 2022) and numerous earthquakes (Senyukov et al., 2009; Thelen et al., 2010; Senyukov, 2013; Koulakov et al., 2021). In particular the LP earthquakes have been observed at two depth ranges : above 5 km and close to 30 km (Gorelchik et al., 2004; Levin et al., 2014; Shapiro et al., 2017a; Frank et al., 2018; Galina et al., 2020). The latter represent the persistent DLP cluster located nearly at the crust-mantle boundary beneath the Klyuchevskoy volcano and possibly associated with a deep magma storage. The temporal correlation between the deep and shallow LP activity has been attributed to the the transfer of the fluid pressure from the deep-seated parts of the magmatic system towards shallow magmatic reservoirs beneath the active volcanoes (Shapiro et al., 2017a; Journeau et al., 2022). Galina et al. (2020) have shown that the frequency–magnitude relationships of these DLP earthquakes deviate from the Gutenberg–Richter power-law distribution, which might indicate an origin different from the regular tectonic earthquakes. Melnik et al. (2020) suggested a possible mechanism related to the rapid degassing of a CO_2–H_2O saturated basaltic magma.

3. Dataset

In this work we use the data of a joint Russian-German-French temporary seismic experiment KISS (Klyuchevskoy Investigation – Seismic Structure of

an Extraordinary Volcanic System) (Shapiro et al., 2017b). The catalog of earthquakes occurred during operation of this network (August 2015 – July 2015) has been compiled by the Kamchatka Branch of Russian Geophysical Survey (Senyukov et al., 2021) based on semi-automatic picking of arrivals of P- and S-waves (Droznin and Droznina, 2011). Earthquakes with the hypocenters located in the vicinity of the crust-mantle boundaries beneath the Klyuchevskoy volcano were selected as potential DLPs. The first choice criterion was the spatial distribution: latitude $\varphi \in [56.0°\text{N}, 56.2°\text{N}]$, longitude $\lambda \in [160.5°\text{E}, 160.7°\text{E}]$ and depth $z > 25$ km. There were 136 events laying within given boundaries. The second criterion $M_L \geq 1.3$ allowed to select 50 strongest earthquakes. Finally, after visually verifying their frequency content and signal-to-noise ratios, we retained 29 earthquakes (Figure 1, Table 1) with waveforms suitable for the analysis of the source parameters recorded at 19 stations. Figure 2 presents an example of a DLP event (No. 6 in Table 1)

4. Hypotheses about the origin and mechanisms of the DLP seismicity beneath the KVG.

A general kinematic description of an earthquake source is based on a moment tensor representation (Aki and Richards, 1980). This second-order symmetric tensor describes generally oriented and shaped discontinuities within the Earth, such as a slip across a fracture plane, or pressure variations within a volume of a nearly spherical shape, of a crack or of a pipe. In addition to moment tensor, the mass advection effects (Takei and Kumazawa, 1994) in mechanically open systems such as volcanic conduits can result in a sin-

gle force component of a seismic source. For example, acceleration of fluid would result in a changing viscous shear force acting on the conduit walls and oriented parallel to the flow (Ukawa and Ohtake, 1987; Shapiro et al., 2018).

Therefore, a most complete description of a seismo-volcanic source could be provided by a combination of a moment tensor and a single force (e.g., Kumagai, 2009). This description contains nine independent parameters (three force components and six independent components of the moment tensor) that can be simultaneously retrieved only in a case of very good data coverage. This situation can be achieved with inversion of very long-period (a few tens of seconds) waveforms recorded by multiple seismic stations (e.g., Ohminato et al., 1998; Chouet et al., 2003, 2005). At such long wavelengths, the propagation of seismic waves (Green's functions) can be predicted with a sufficient accuracy based on 3D numerical simulation with accounting for topography and other effects.

At shorter periods, full waveform inversion becomes problematic because of the difficulty to characterize the wave propagation accurately. In this case, the source configurations are inferred from a reduced set of parameters measured from amplitudes and phases of the waveforms. Very often, kinematic source mechanisms are constrained with the polarities of first arriving P-waves. In the case of volcanic DLP earthquakes this approach is, however, problematic because the relatively weak DLP signals emerge from the noise only after band-pass filtering the raw seismograms. In particular, the strong microseismic noise is removed with high-pass filters with corner frequency near 1 Hz, which is very close to the dominant frequencies of LP waveforms.

As a result, phases of filtered waveforms can be strongly distorted and their apparent polarities reversed.

Therefore, in this study we use the amplitude information and namely the distribution of S-to-P amplitude ratios. This type of observation has been shown to provide useful constraints on focal mechanisms and has been used in some previous studies of DLP earthquakes (e.g., Ukawa and Ohtake, 1987; Ohmi and Obara, 2002; Nakamichi et al., 2003; Ikegaya and Yamamoto, 2021). At the same time it is associated with strong uncertainties (Hardebeck and Shearer, 2003) because of the noise and site amplifications. Taking these circumstances into consideration, we do not set up a full inversion for an arbitrary focal mechanism with 9 free parameters that would be highly unstable and non-unique. Instead, we test specific hypotheses about possible DLP generation processes. Each hypothesis is related with a "simplified" focal mechanism depending on a reduced number of parameters (maximum three).

One possibility is that DLP earthquakes are caused by the release of mechanical stresses in the crust beneath volcanoes that can be accommodated as a slip on faults. The shear-fault mechanism is described by three angles (Figure 3a). The azimuth ϕ and the dip angle δ define the fault plane orientation, and the rake λ points the direction of the slip.

The DLP earthquakes can be caused by rapid magma pressure variations. The associated kinematic source mechanism will then depend on the shape of a magma filled volume. The most efficient mechanism of magma transport through the cold crust is via formation of cracks along which magma flows in the form of dikes and sills (e.g., Rubin, 1995; Melnik et al., 2022). Pressure

variations in such planar intrusion can be approximated by a tensile crack mechanism. It can be oriented in space with a normal vector to a crack surface (Figure 3b), thus it is described with two angles: the azimuth ϕ and the polar angle (dip) θ. A similar kinematic mechanism will describe the opening of tensile cracks (e.g., Bean et al., 2014).

Pipe-shaped magmatic conduits are formed beneath eruptive vents of volcanoes. We consider a possibility of such conduits at depth. A pressure variation within such conduit is kinematically described as a cylindrical pipe whose orientation is also defined by two angles, the azimuth ϕ and the dip θ (Figure 3c).

Finally we consider a situation when acceleration of magma within a conduit can result in traction forces (Ukawa and Ohtake, 1987; Shapiro et al., 2018). Such single-force mechanism is described by two angles, the azimuth ϕ and the dip θ, defining the force vector (Figure 3d).

5. Estimation of the DLPs source mechanism with S-to-P amplitude ratios

In this approach, we first compute theoretical ratios between the amplitudes of P- and S-waves and thereafter compare them with those measured from the real seismograms.

5.1. Calculation of the theoretical S-to-P amplitudes ratios.

We start with theoretical expressions of far-field P- and S-wave displacements in a homogeneous isotropic media characterized by density ρ, P-wave velocity α, and S-wave velocity β (Aki and Richards, 1980). For a source described by a single force $\mathbf{F}$, the wave amplitudes on component i are:

$$u_i^P = \frac{F_j R_{i,j}^{FP}}{4\pi\rho\alpha^2 r} \tag{1}$$

$$u_i^S = \frac{F_j R_{i,j}^{FS}}{4\pi\rho\beta^2 r} \tag{2}$$

where F_j is the force projection on direction j, r is the distance between the source and the receiver, and $R_{i,j}^{FP}$ and $R_{i,j}^{FS}$ are the force-type radiation patterns for P- and S-waves that are expressed via the directional cosines of a vector pointing from the source to the station γ:

$$R_{i,j}^{FP} = \gamma_i \gamma_j \tag{3}$$

$$R_{i,j}^{FS} = \delta_{i,j} - \gamma_i \gamma_j \tag{4}$$

For a source described by a seismic moment rate tensor $\dot{\mathbf{M}}$, these expressions become:

$$u_i^P = \frac{\dot{M}_{j,k} R_{i,j,k}^{MP}}{4\pi\rho\alpha^3 r} \tag{5}$$

$$u_i^S = \frac{\dot{M}_{j,k} R_{i,j,k}^{MS}}{4\pi\rho\beta^3 r} \tag{6}$$

where $R_{i,j,k}^{MP}$ and $R_{i,j,k}^{MS}$ are the moment-type radiation patterns that are also expressed via the directional cosines γ (Aki and Richards, 1980). Details about representations of different types of elementary sources and computation of radiation patterns are given in Appendix A.

For known source and station positions the direction from the source to the station (azimuth φ and polar angle i_ξ) can be evaluated (i.e., with ray

tracing). Based on this, directional cosines and radiation patterns can be computed and displacement components predicted with equations (3-4) or (5-6).

In some studies (e.g., Ukawa and Ohtake, 1987; Ikegaya and Yamamoto, 2021), a correction of the free surface effect is also introduced. It is computed separately for P-, SH- and SV-waves and requires assumption about the velocity models and estimations of the incident angles at different stations, which can be highly uncertain. Therefore, considering the relatively deep location of the source and the significant velocity gradient in the crust, we assume the incidence of waves is close to vertical at all stations. Another suggested correction (e.g., Ukawa and Ohtake, 1987) is aimed to account for the difference in the attenuation for P- and S-waves. This difference is rather pronounced at relatively low frequencies where the S-wave quality factor is significantly lower that the one for the P-waves. However, for waves with frequencies higher than 1 Hz propagating in the Earth's crust, the seismic attenuation is dominated by the scattering resulting in a reverse situation with the quality factor of P-waves being lower than one of S-waves (e.g., Sato, 1984). Measurements of the high-frequency P- and S-wave quality factors in the crust (e.g., Campillo and Plantet, 1991; Yoshimoto et al., 1993) produced a wide range of values showing that on average their ratio is not very different from the V_P/V_S ratio. In this situation, the distance dependent attenuation of P- and S-waves remains nearly identical. This scattering regime in the crust corresponds well to the DLP emitted waves. Therefore, we do not apply the attenuation correction.

With the considerations described above, full displacements of P- and

S-waves are expressed as:

$$A_P^{calc} = \sqrt{(u_x^P)^2 + (u_y^P)^2 + (u_z^P)^2}$$
$$A_S^{calc} = \sqrt{(u_x^S)^2 + (u_y^S)^2 + (u_z^S)^2} \quad (7)$$

and their ratios can be simply computed and compared with the observations.

5.2. Measuring S-to-P amplitudes ratios from real seismograms.

Before measuring real observed amplitudes, seismograms were preprocessed with removing instrument response and filtering them in 1–4 Hz frequency band (Figure 4a). Instead of measuring amplitudes of P- and S-waves separately at different channels, these values were obtained after calculating the 3-component amplitude as:

$$u^{3C} = \sqrt{u_N^2 + u_E^2 + u_Z^2} \quad (8)$$

Then, we smooth the amplitude with a 1 s moving window (Figure 4b). The resulting envelope was manually processed in order to limit time intervals of P- and S-waves arrivals (black and red dashed lines in Figure 4b correspondingly) and then pick A_P and A_S as maximum values within defined time intervals.

5.3. Correction for the site amplifications.

Raw A_S/A_P measurements shown in Figure 4b contain some very elevated values. The reason for this is that they are strongly affected by site amplifications. Because of the geological structure of the studied area with the majority of its territory covered by soft sediments of very recent volcanic

deposits (Green et al., 2020), most of sites on which the stations of the KISS experiment were installed are prone to strong amplification of seismic waves. This amplification does not affect equally the P- and the S-waves, which can introduce a significant bias into raw A_S/A_P measurements.

Therefore, we estimated the site amplifications for P- and S-waves separately and used these estimations to correct the amplitude ratio measurements. Details of this analysis are described in Appendix B. The S-wave amplification factors were estimated from coda of relatively strong regional earthquakes. For P-waves, we used a few earthquakes occurred approximately beneath the network. The site amplification measurements are summarized in Table B.4. After computing the average amplification factors for each station AF_S^i and AF_P^i, we correct the raw measurements as:

$$\lg\left(\frac{A_S}{A_P}\right)_i^{obs} = \lg\left(\frac{A_S}{A_P}\right)_i^{raw} - \lg\left(\frac{AF_S^i}{AF_P^i}\right) \tag{9}$$

An example of corrected measurements at a single station is shown in Figure 4b. Logarithms of amplitude ratios before and after removing site amplification at all stations are presented in left and right panels of Figure 5 correspondingly.

5.4. Comparison of the observed and calculated amplitude ratios

We study source mechanisms of the earthquakes located by Senyukov et al. (2021). For a known source location and a fixed mechanism orientation ξ (that can be determined by two or three angles depending on the considered source type, Appendix A), a residual between observations and a model at station i is estimated as L_1 norm:

$$\Delta_i(\xi) = \left| \lg \left(\frac{A_S}{A_P} \right)_i^{obs} - \lg \left(\frac{A_S(\xi)}{A_P(\xi)} \right)_i^{calc} \right| \tag{10}$$

And the overall misfit function over the entire network of stations is:

$$M_{L_1}(\xi) = \frac{1}{N_{st}} \sum_{i=1}^{N_{st}} \Delta_i(\xi) \tag{11}$$

To find the minimum of the misfit function, we perform a grid search in the domain of the mechanism orientations ξ. For mechanisms determined with two angles, the grid is designed to distribute the points homogeneously over the hemisphere (Appendix C, Figure C.20). The third parameter (rake angle in the case of a shear-slip source and component ratio in the case of source represented by a combination of a horizontal crack and a force) was sampled homogeneously to construct a three dimensional grid (Appendix C, Figure C.21).

6. Results

6.1. An example of a single DLP earthquake

We start with showing the source inversion results for a DLP earthquake occurred on August 20, 2015 at 12:23:54. Its seismograms are presented in Figure 2 and distribution of observed amplitude ratios in Figure 5. Figure 6 shows the comparison of the observed logarithms of amplitude ratios with those computed for the best-fitting orientations for the different mechanisms. Table 2 also contains the values of observed and calculated logarithms of ratios as well as the residuals at all stations as shown in Figure 6. The corresponding distributions of the misfits as a function of orientation angles are shown in Figure 7.

The results of the inversion for the considered earthquake show that the shear-slip mechanism can be reasonably excluded because its misfit (Figure 7a) is more than 40% larger than those of other types of "elementary" mechanisms (Figures 7b-d). This difference is especially significant considering that the slip mechanism is described by three free parameters while all other only by two.

Among other elementary mechanisms, those with volumetric changes, i.e., tensile crack (Figure 7b) and cylindrical pipe (Figure 7c), have slightly better (5-9%) misfits that the sinle force (Figure 7c) , with a slight advantage for the tensile crack over the pipe. However, the misfit distribution as a function of orientation angles for the crack mechanisms is very irregular. Additionally, all minima of this distribution are rather far from the center, i.e., from the horizontally oriented sill. Such horizontally oriented structures could expected beneath Klyuchevskoy in association with the near-Moho magmatic reservoir (Levin et al., 2014) likely formed by underplating (Annen et al., 2005).

Therefore, we also test a configuration when a sudden pressure increase within a horizontal sill is released in connected conduit through which it pushes the magma resulting in a viscous drag force (Ukawa and Ohtake, 1987). Such "complex" source modeled as a combination of a horizontal tensile crack and arbitrary oriented single force results in the overall best misfit among all considered mechanisms. At the same time its description requires three free parameters: two force angles and a scaling coefficient between the force and the crack components (Equation 12), making its apparent advantage less significant.

$$r = \frac{A_{crack}}{A_{crack} + A_{force}} \tag{12}$$

Overall, we can conclude the DLP mechanisms contain a significant volumetric and/or single-force component. At the same time, the difference between different mechanisms with such components is not sufficient to unambiguously select one of the scenarios. Moreover, the distributions of the misfit values in the source parameters space may contain several minima (Figure 7) making the final inference highly uncertain. This confirms the assessment from some previous studies (Hardebeck and Shearer, 2003) that the information contained in the S-to-P amplitude ratios is too uncertain to constrain the details of individual source mechanisms. Therefore, we try to make inferences based on the analysis of all sufficiently strong DLP earthquakes recorded during the KISS experiment.

6.2. Application to all selected DLP earthquakes

29 selected DLP earthquakes (Table 1) were recorded by minimum 9 and maximum 19 stations (Figure 8) depending on the signal-to-noise ratio of signals and data availability. Figure 9a shows the values of misfit functions estimated for different types of mechanisms for the selected DLP earthquakes. The average values for each mechanism type are shown in the box of Figure 9a.

Because the tested source models contain different number of parameters, the misfits were recalculated into Akaike information criteria (AIC) following (Ikegaya and Yamamoto, 2021):

$$\mathrm{AIC} = N_{st} \ln(2\pi) + N_{st} \ln(M_{L_1}^2) + N_{st} + 2(m+1) \tag{13}$$

where N_{st} is a number of stations (from 9 to 19), $M^2_{L_1}$ is a misfit value and m is the number of parameters in a model (2 for crack, pipe and force and 3 for the the shear slip and combined mechanisms). The obtained AIC values for selected DLPs are shown in Figure 9b. It can be seen that the shear fault mechanism still have the highest AIC values and can, therefore, be excluded from the further analysis.

On the next step we analyze the consistence of the inferred source parameters over the ensemble of studied earthquakes. For a single force mechanism, the both angles defining its orientation remain quite stable in time as shown in Figure 10. On average, they correspond to a force directed to the south-southwest and inclined ∼40 degrees relative to the vertical with standard deviations of 15° and 7° for the azimuth and dip angles, respectively.

While these angles are more scattered (standard deviations of 43° and 18° for the azimuth and dip angles, respectively) for the pipe mechanism (Figure 11), its average southward orientation can still be deduced. The inferred angles of tensile cracks vary very strongly (standard deviations of 91° and 17° for the azimuth and dip angles, respectively) between different individual DLP earthquake (Figure 12) and no preferred average orientation could be traced.

For the "combined" source (Figure 13), the force south-southwest azimuth remain highly stable (standard deviations of 24°) while the polar angle exhibits considerable scattering (standard deviations of 12°). Variations of the DLP source parameters in time may reflect the variability of the underlain physical process. Alternatively, these variations could be related to the unstable inversion procedure. As shown in the previous section (Figure 7),

positions of the misfit minima in the parameter space are poorly constrained for a single DLP earthquake for such mechanisms as the tensile crack or the pipe which could be the cause of the observed "apparent" variation of the source parameters in time.

6.3. Stacked misfit distributions

If the generation of the DLP earthquake is related to the preferential magma pathways, these later might be expected relatively stable and not varying strongly over short times. Such time stationarity of the DLP generating mechanism is partially confirmed by the high level of similarity of their waveforms over series of many events, i.e., the multiplet behavior (Shapiro et al., 2017a). To test the hypothesis of stationary processes of generation of DLP earthquakes, we decided to compute "stacked" misfit distributions for all selected events ($N_{DLP} = 29$):

$$M_{L_1}^{stack}(\phi,\theta) = \frac{1}{N_{st}^{cum}} \sum_{i=1}^{N_{DLP}} N_{st}^{i} \cdot M_{L_1}^{i}(\phi,\theta) \tag{14}$$

where $M_{L_1}^{i}(\phi,\theta)$ is a misfit distribution in the azimuth-polar angle plane corresponding to one of 29 selected DLPs (i.e., Figure 7). N_{st}^{i} is a number of stations used for DLP i. $N_{st}^{cum} = \sum_i N_{st}^{i}$ is the total number of used seismic records. For the "elementary" source mechanisms, equation 14 implies a simple stacking in the polar coordinate plane. For the combined sill-force source, an additional degree of freedom is still present because the third parameter r (equation 12) is allowed to vary for different event and angles. Physically, this would correspond to a situation when the geometry of the DLP generating part of the plumbing system remains fixed and the partitioning of energy

between the pressure increase in the sill and the viscous drag in the conduit can be variable between different DLP earthquakes.

Figure 14 show the distributions of "stacked" misfits for different source mechanisms. In comparison with the results for separated DLP earthquakes (Figures 7 and 9) the minimum misfit values remain similar, implying that the consistency of whole ensemble of observations is at the same level as for individual events. The misfit distributions did not change significantly for the single force and "combined" mechanism indicating the preferential south-southwest direction. The distribution has been "stabilized" (the minima more clearly defined) for the pipe mechanism and shows more clearly the southward orientation. The "tensile crack" solution still remain unstable with showing several misfit minima with close values. In terms of the absolute misfit minima values, the best solution are obtained with the pipe and combined source mechanisms.

7. Discussion and Conclusions

Understanding physical processes leading to generation of DLP earthquakes remains an elusive task. Inferring their kinematic source mechanisms based on observed seismic waveforms could provide a key constraint to discriminate between different existing hypotheses. With this in mind, we explored the records of 29 DLP earthquakes by broadband stations of the KISS temporary seismic experiment in the region of the Klyuchevskoy volcanic group in Kamchatka, Russia (Shapiro et al., 2017b).

We first argued that the methods based on the phase of seismograms (inversion of full waveforms of polarities of first arrivals) are not practical

in the case of DLP earthquakes because their relatively weak signals emerge from the noise only after band-pass filtering. In particular, the strong microseismic noise is removed with high-pass filters with corner frequency near 1 Hz, which is very close to the dominant frequencies of LP waveforms. As a result, phases of filtered waveforms can be strongly distorted and their apparent polarities reversed.

Consequently, we explored a method based on the amplitude measurements. Namely, as has been suggested in some previous studies, we use the amplitude ratios of P- and S-waves (e.g., Ukawa and Ohtake, 1987; Ohmi and Obara, 2002; Nakamichi et al., 2003; Ikegaya and Yamamoto, 2021). This type of measurement can be biased by possibly different surface site amplification of P- and S-waves. We implemented a correction for this effect with measuring S-wave and P-wave site amplifications (Appendix B) from a few regional earthquakes well recorded by the whole network. The estimated correction factors result on average decrease of the raw S-to-P amplitude ratios and are subject to significant uncertainties. Additional uncertainties in the inversion of the amplitude data arise from the only approximately known model of the wave propagation.

The mentioned uncertainties in the data and in the forward model contribute to the non-uniqueness of the inversion procedure. To mitigate this non-uniqueness, we decided to consider source models with a limited number of free parameters. So far, a complete kinematic description of a volcanic earthquake source would be obtained with a combination of a moment tensor and a single force (e.g., Kumagai, 2009), which would require nine independent parameters (three force components and six independent components of

the moment tensor). Considering the limitations of our amplitude measurements, instead of trying to resolve all these parameters simultaneously, we test a set of simplified source mechanisms (involving 2 or 3 parameters) that represent "elementary" physical processes that may generate seismic waves: (1) slip on faults, (2) magma pressure variation within sills, dykes, or pipe-shaped conduits, and (3) viscous drag force caused by acceleration of magma flow in a conduit.

Even with such a reduced number of parameters, the inversion of individual DLP earthquakes remains non-unique for most of types of mechanisms which is manifested by multiple minima in the misfit distributions (Figure 7). To further stabilize the inversion, we consider the hypotheses of time stationarity of the DLP generating processes based on which we invert measurements for all studied DLP earthquakes simultaneously (via stacking the misfit distributions obtained for individual events). As a result of this procedure, the best-misfit levels are not deteriorated indicating the reasonable likeliness of a single mechanism explaining all observations. The misfit distributions show relatively well defined minima for all mechanisms except the tensile crack.

Comparison of the minimum misfit levels for different types of studied mechanisms allows us to conclude that the generation of DLP earthquakes beneath the Klyuchevskoy volcano by slip on faults is not consistent with the observed S-to-P amplitude ratios whose explanation requires mechanisms with volumetric or single force components. For such mechanisms (tensile crack, pipe, and single force) the difference in misfit to seismic data is not very strong. This implies that seismic data alone is not sufficient to unam-

biguously constrain the details of the source mechanisms. At the same time, the plausibility of results of different seismic inversions can be interpreted based on some additional hypotheses about the functioning of the KVG volcano plumbing system.

So far, there are two reasons to consider that solutions obtained with a pure tensile crack mechanism are less likely (even if they cannot be definitely excluded). First, the strong difference in solutions for individual events (Figure 12) is not consistent with the time stationarity that may be expected for the geometry of plumbing system. Second, the average and most individual best-fit solutions correspond to significantly dipping structures while in the vicinity of the crust-mantle boundary nearly horizontal sills are more likely.

Results of inversion for the three remaining tested mechanisms show some consistency. Namely, they all indicate a south-southwest dipping magmatic conduit generating either pipe-shaped pressure perturbations or an along-conduit force. This leads to a possible interpretation shown in Figure 15. The DLP earthquakes are generated near the crust-mantle boundary (Moho) approximately beneath the Klyuchevskoy volcano, where the main deep magmatic reservoir feeding the KVG volcanoes is located (e.g., Levin et al., 2014). This magma storage is likely shaped as complex of underplated sills. From this deep reservoir magma penetrates the crust through a south-southwest dipping conduit (or a system of conduits). This orientation of dominant magma pathways would be in agreement with the overall interconnection of the transcrustal KVG plumbing system when the pressure perturbations in the deep reservoir are transmitted not only to Klyuchevskoy but also to the active volcanoes located south of it, Bezymianny and Tolbachik (Fedo-

tov et al., 2010; Shapiro et al., 2017a; Coppola et al., 2021; Journeau et al., 2022).

Acknowledgements

This study was financially supported by the European Research Council (ERC) under the European Union Horizon 2020 Research and Innovation Program (grant agreement 787399-SEISMAZE). KISS dataset (doi:10.14470/K47560642124) is available from the GEOFON data center of GFZ-Potsdam (https://geofon.gfz-pots-dam.de/).

Credit author statement

Nataliya Galina: Conceptualization, Software, Formal analysis, Investigation, Visualisation, Writing - Original draft preparation **Nikolai Shapiro**: Conceptualization, Methodology, Validation, Writing - Review and Editing.

Competing interests

The authors declare that they have no financial or other competing interests.

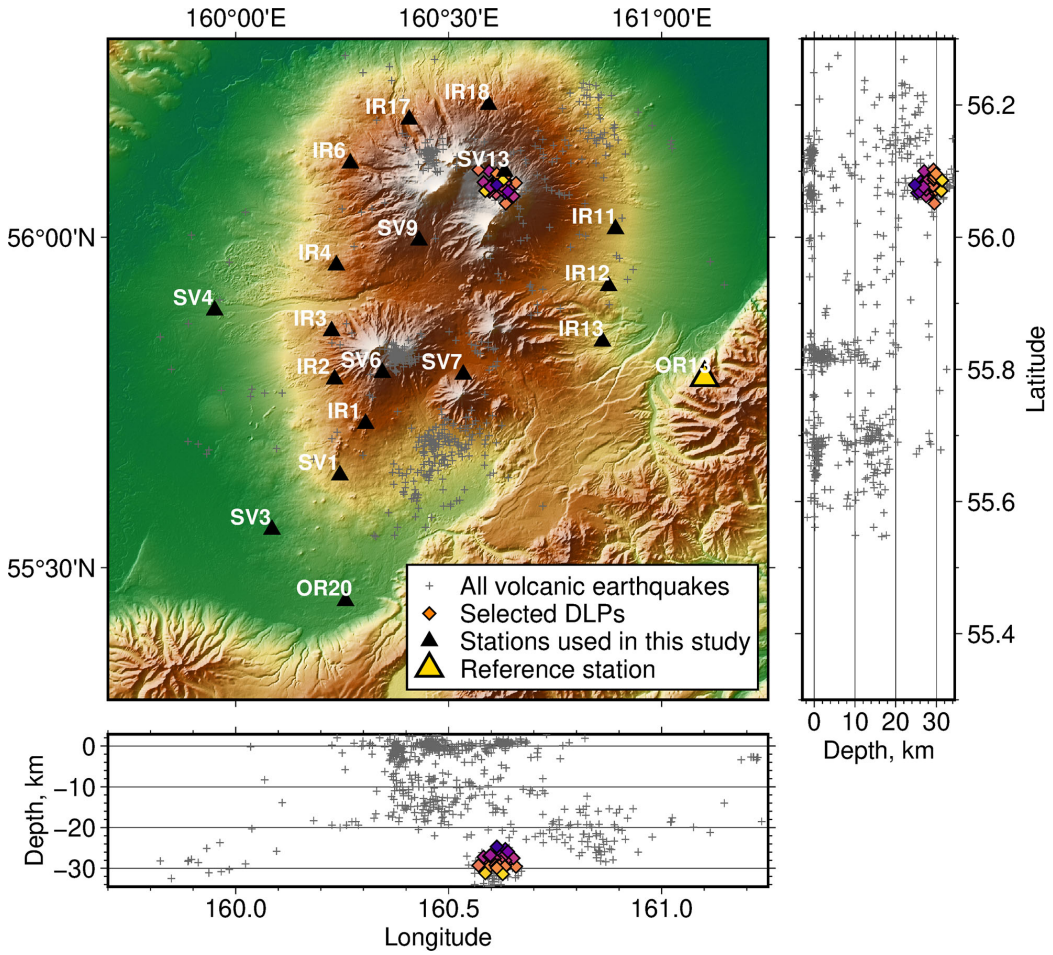

Fig. 1: Map of the Klyuchevskoy volcano group. The stations used in this work are represented by black triangles. The "reference" station OR13 is additionally highlighted with yellow color. Grey crosses show the entire catalog of volcanic earthquakes with approximately crustal depth recorded beneath the KVG during the KISS experiment (Senyukov et al., 2021). Colored diamonds show hypocenters of the DLP earthquakes selected for this study.

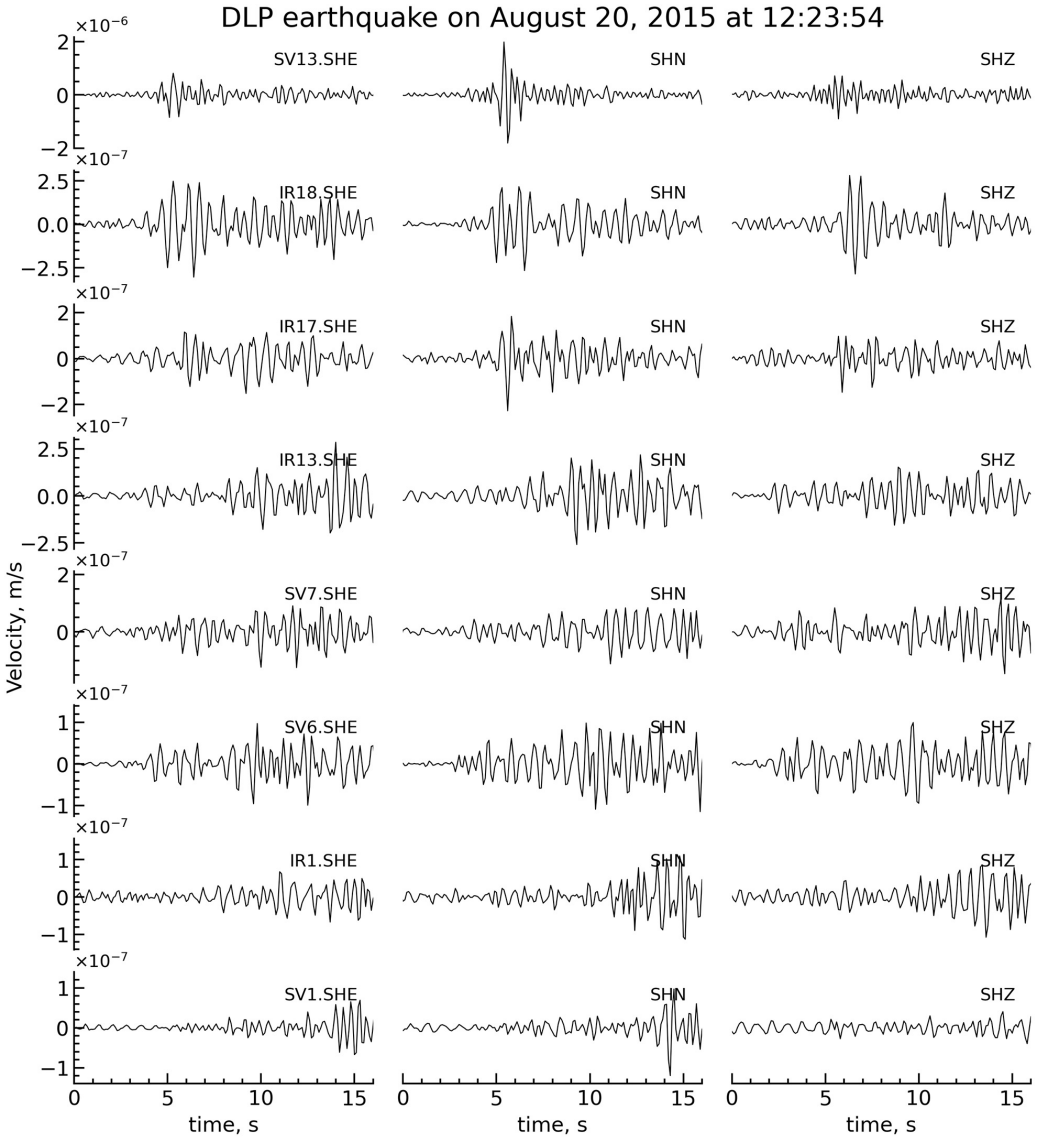

Fig. 2: Example of sesimograms recorded by multiple KISS stations during a DLP earthquake occurred on August 20, 2015 at 12:23:54.

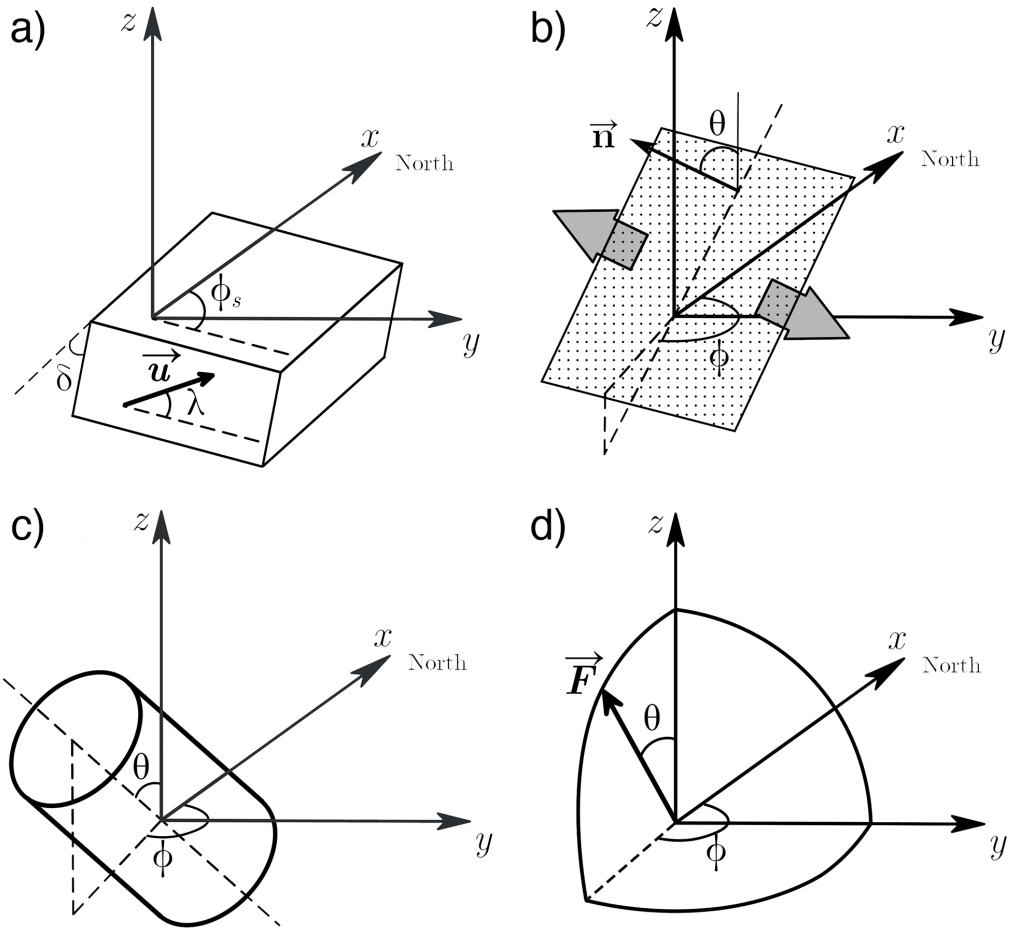

Fig. 3: Considered "elementary" source mechanisms and respective angles required for their description: (a) a shear slip on a fault (strike $\phi_s \in [0°, 360°]$, dip (polar angle) $\delta \in [0°, 90°]$, rake $\lambda \in [-180°, 180°]$) (b) a tensile crack (azimuth $\phi \in [0°, 360°]$, dip $\theta \in [0°, 90°]$) (c) a cylindrical pipe (azimuth $\phi \in [0°, 360°]$, dip $\theta \in [0°, 90°]$) (d) a single force (azimuth $\phi \in [0°, 360°]$, dip $\theta \in [0°, 90°]$)

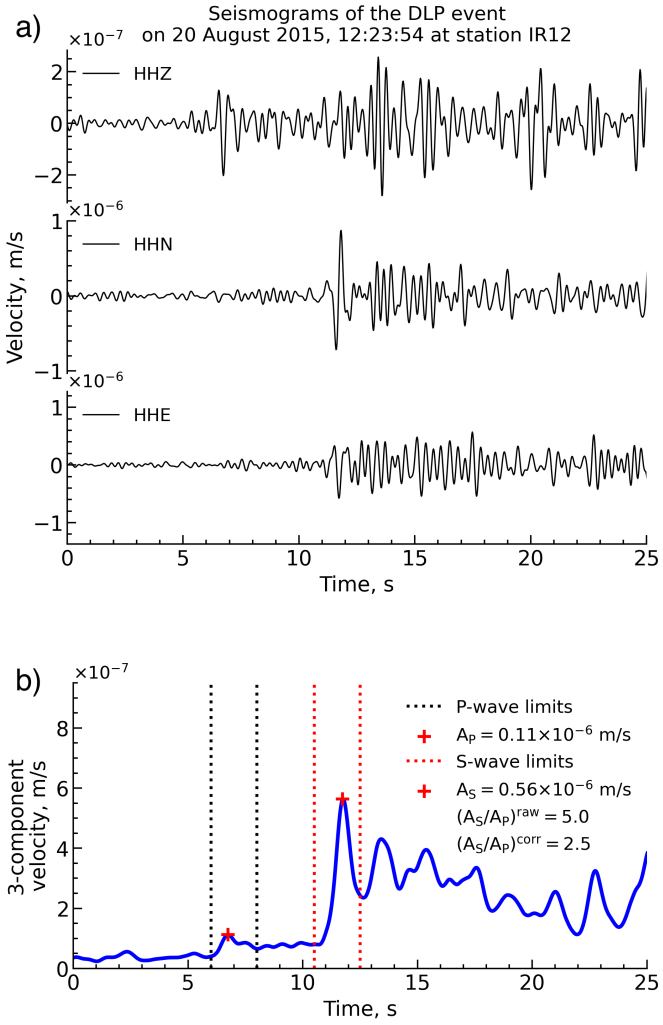

Fig. 4: Example of measurements of P- and S-waves amplitudes for the DLP event on August 20, 2015 at 12:23:54 at station IR12. a) Seismograms after removing the instrument response and band-pass filtering (1–4 Hz). b) A three-component amplitude envelope smoothed with a 1 s window. Black and red vertical dotted lines indicate windows used for P- and S-waves. Maxima for P- and S-waves are indicated with red crosses.

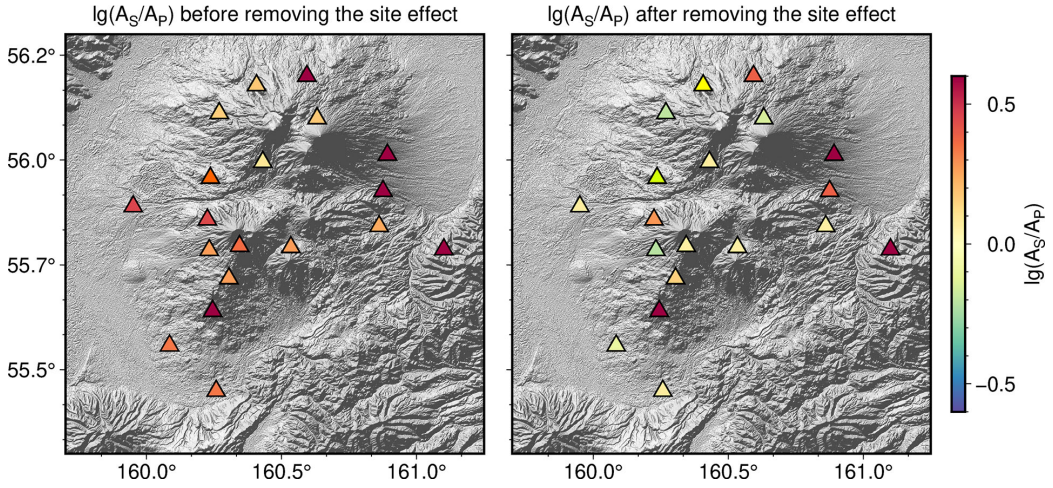

Fig. 5: S-to-P amplitude ratios measured at various stations for a DLP earthquake occurred on August 20, 2015 at 12:23:54. (a) Raw measurements (b) Values after correcting for the site amplification.

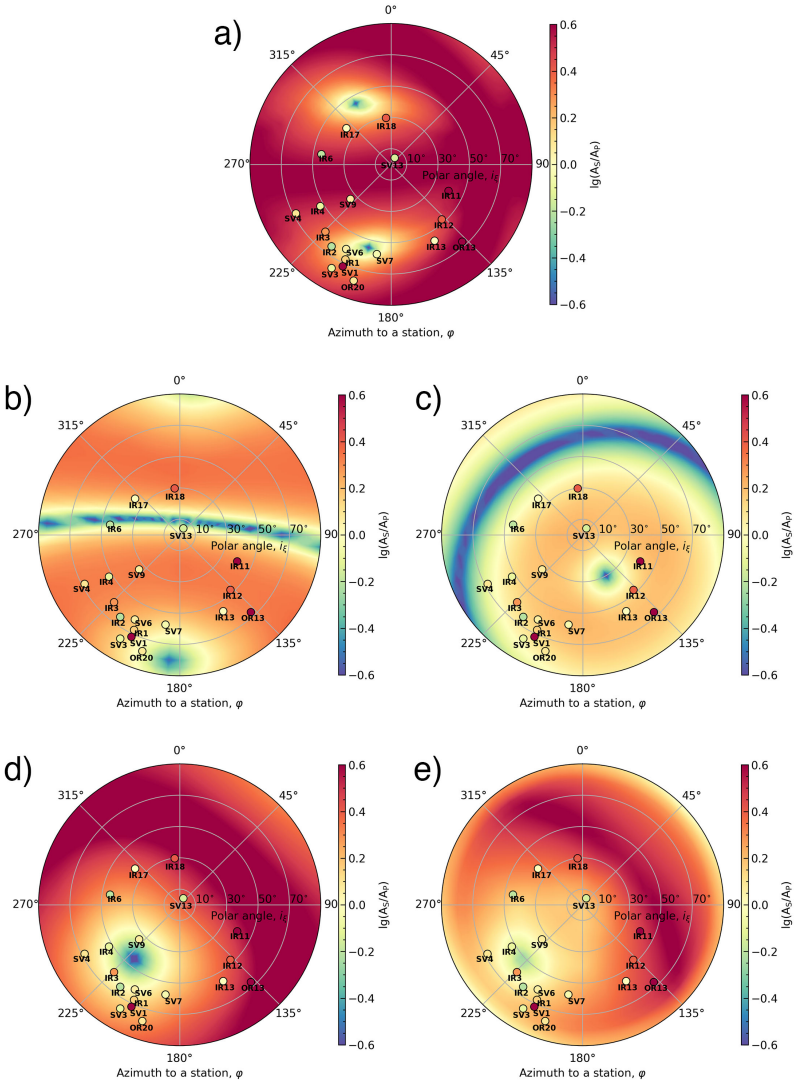

Fig. 6: Distribution of computed logarithms of amplitude ratios and observed values at stations (shown in circles with corresponding codes) for best-fit orientations of considered source mechanisms (an example on a DLP on August 20, 2015 at 12:23:54). (a) Shear fault: strike $\phi_s = 85°$, dip $\delta = 84°$, rake $\lambda = 66°$; (b) Tensile crack: azimuth $\phi = 184°$, dip $\theta = 81°$; (c) Cylindrical pipe: azimuth $\phi = 150°$, dip $\theta = 30°$; (d) Single force: azimuth $\phi = 220°$, dip $\theta = 45°$; (e) Combination of a horizontal tensile crack and a single force with orientation: azimuth $\phi = 228°$, dip $\theta = 51°$;

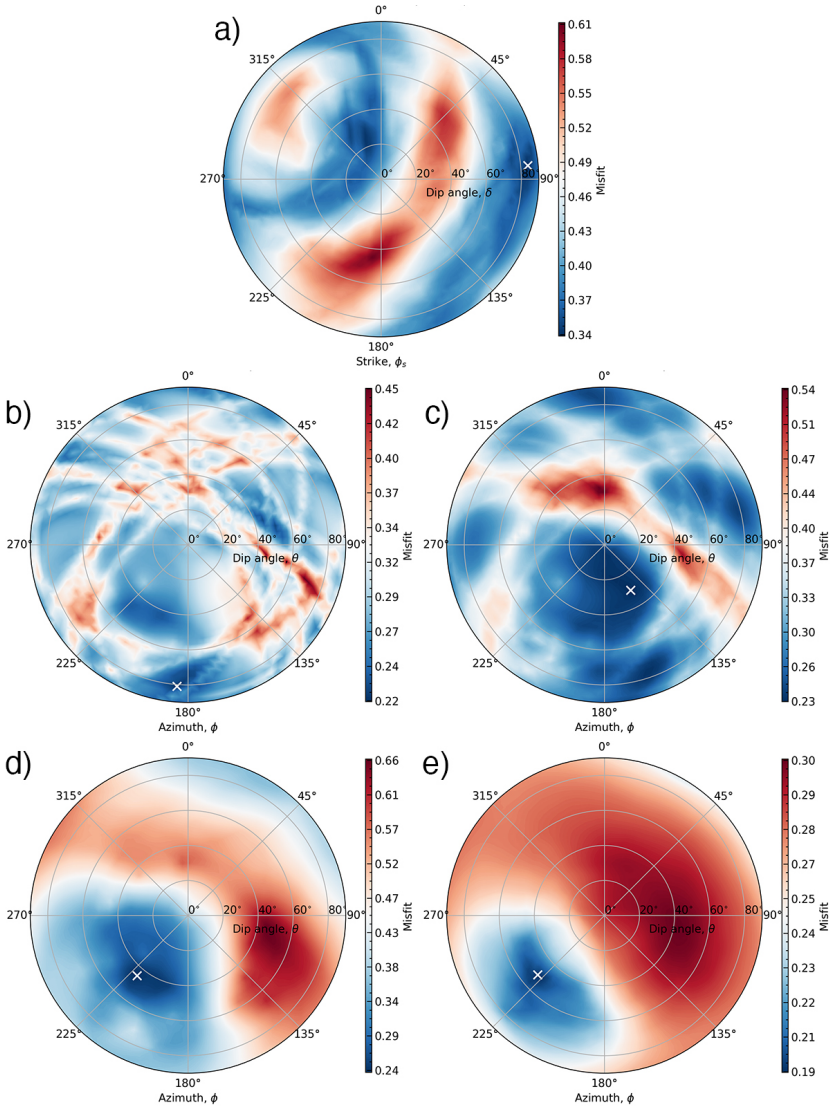

Fig. 7: Distribution of misfits for considered source mechanisms (example of a DLP earthquake on August 20, 2015 at 12:23:54). Minima of misfits are shown with white crosses and have the following values: (a) Shear fault $M_{L_1} = 0.34$; (b) Tensile crack $M_{L_1} = 0.22$; (c) Cylindrical pipe $M_{L_1} = 0.23$; (d) Single force $M_{L_1} = 0.24$; (e) Combination of a horizontal tensile crack and a single force $M_{L_1} = 0.19$

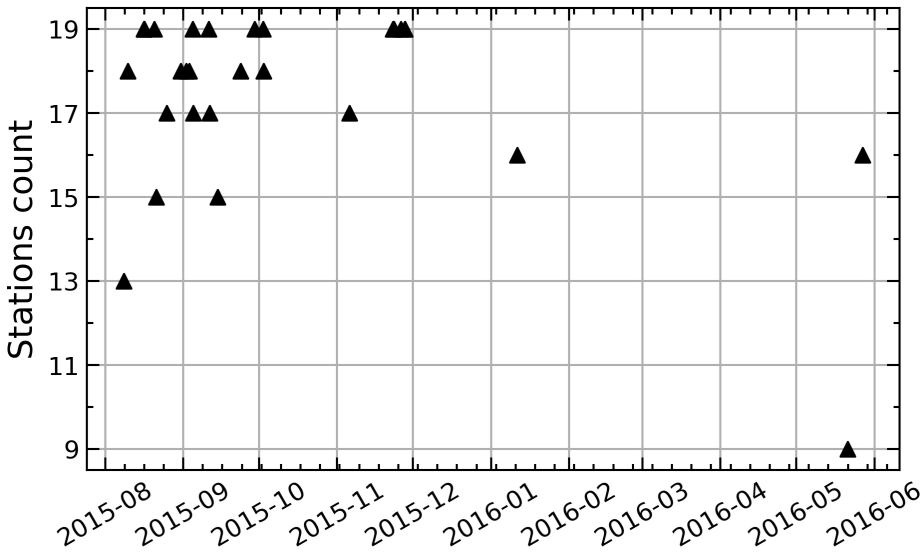

Fig. 8: The number of stations used in processing of each of the selected DLPs.

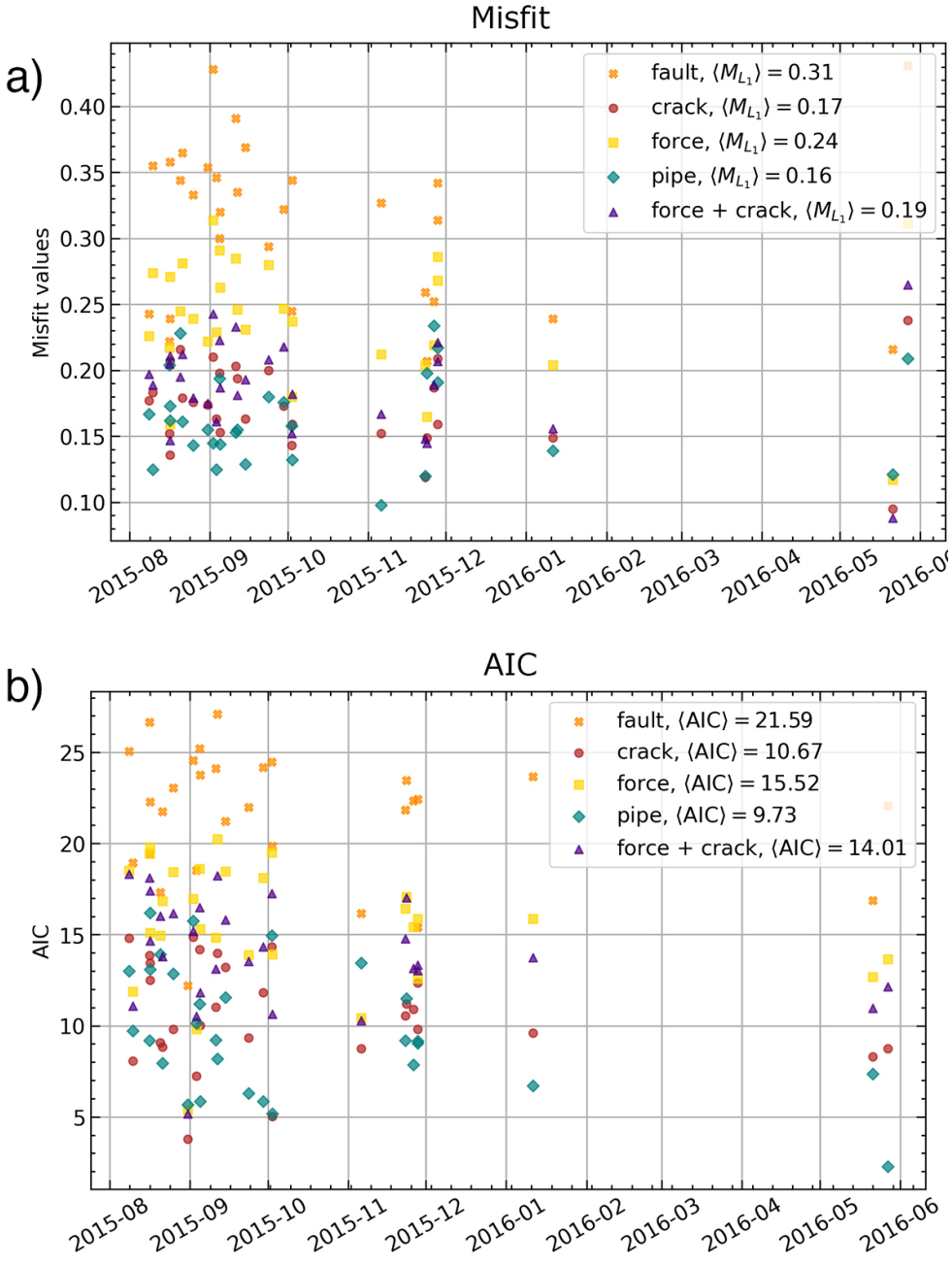

Fig. 9: Distributions of (a) misfits and (b) AIC values in time depending on the chosen source mechanism (shown with different colors and markers as indicated in the legend).

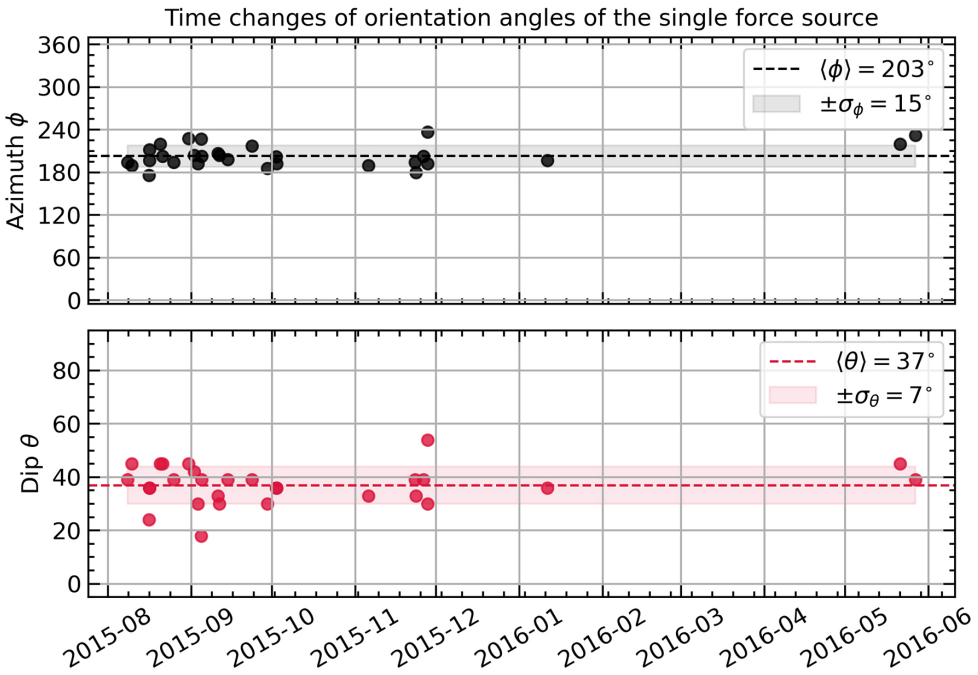

Fig. 10: Temporal changes of the orientation of a single force vector in space: (a) Azimuth $\phi = 203^\circ \pm 15^\circ$ (b) Dip angle $\theta = 37^\circ \pm 7^\circ$. Average values and standard deviations are shown by dashed lines and colored areas, respectively

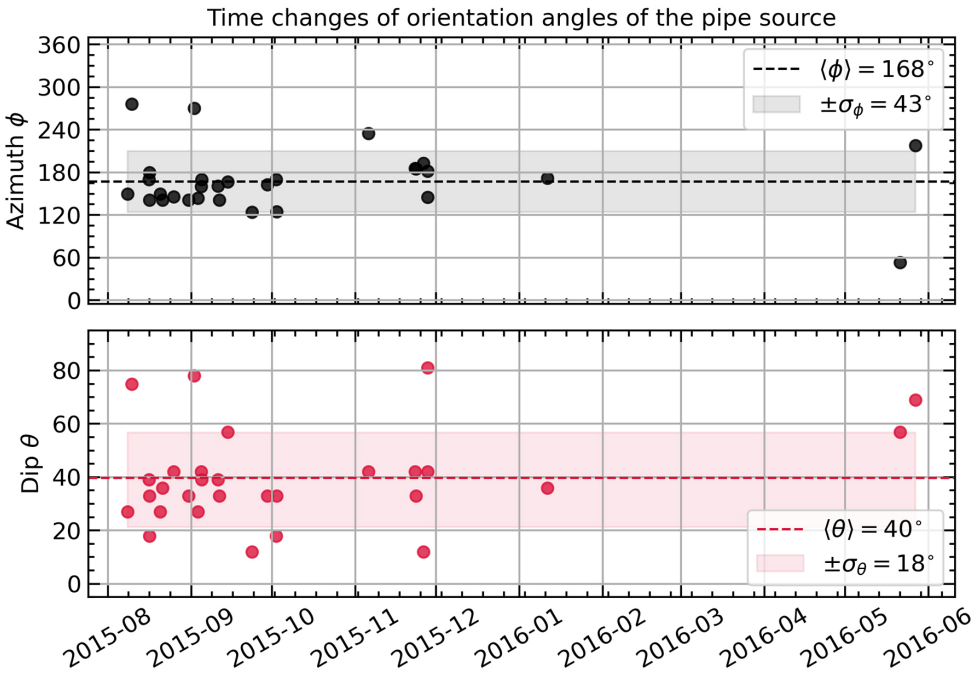

Fig. 11: Temporal changes of the orientation of a cylindrical pipe axis: (a) Azimuth $\phi = 168^\circ \pm 43^\circ$ (b) Dip angle $\theta = 40^\circ \pm 18^\circ$. Average values and standard deviations are shown by dashed lines and colored areas, respectively.

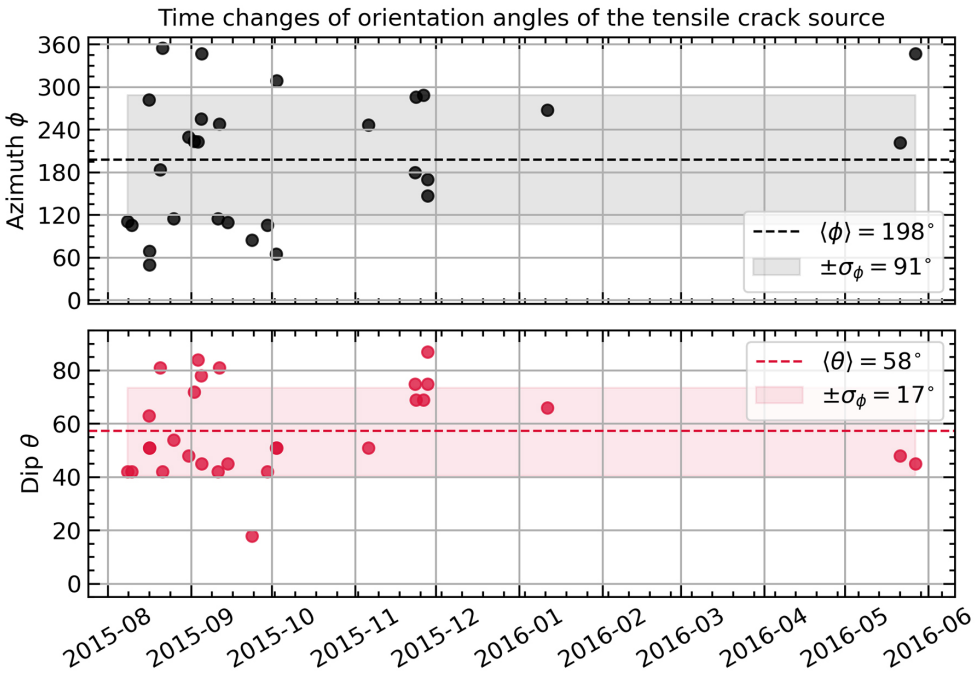

Fig. 12: Temporal changes of the orientation of the normal to a tensile crack surface: (a) Azimuth $\phi = 198^\circ \pm 91^\circ$ (b) Dip angle $\theta = 58^\circ \pm 17^\circ$. Average values and standard deviations are shown by dashed lines and colored areas, respectively.

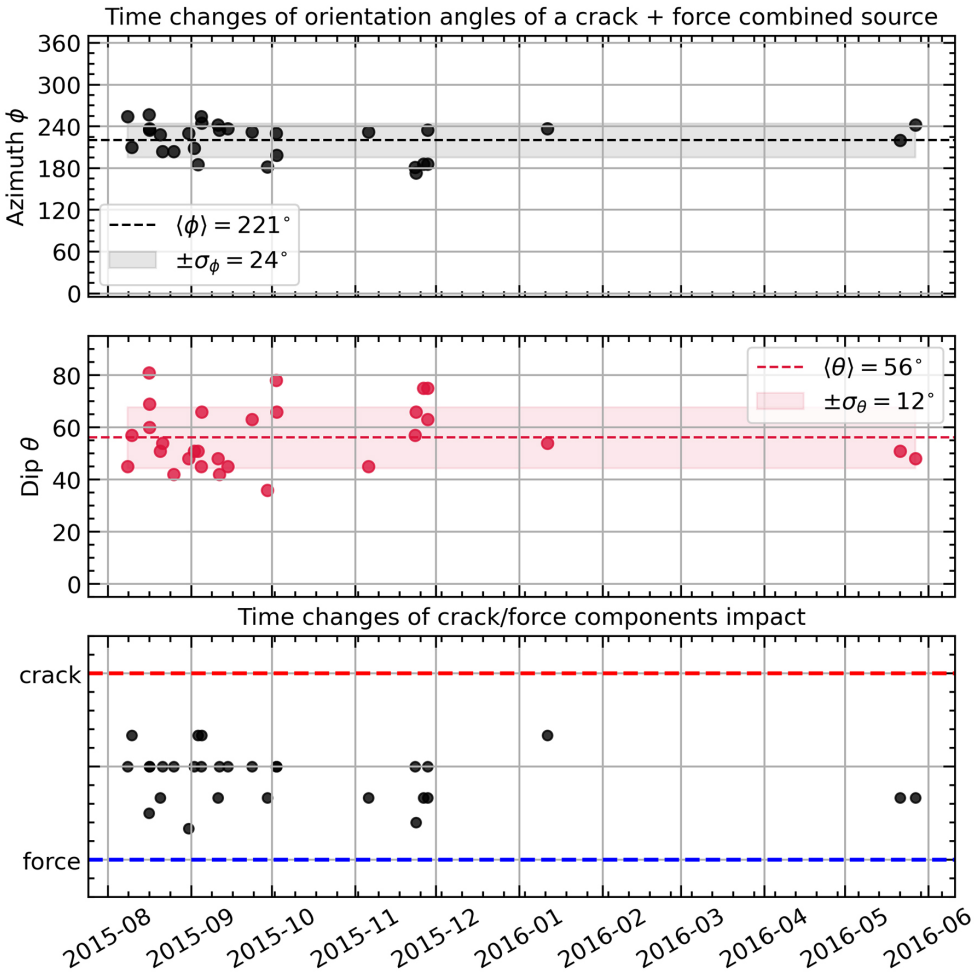

Fig. 13: Temporal changes of the vector orientation of a single force compound of a "combined" source in space: (a) Azimuth $\phi = 221^\circ \pm 24^\circ$ (b) Dip angle $\theta = 56^\circ \pm 12^\circ$. Average values and standard deviations are shown by dashed lines and colored areas, respectively. (c) Temporal changes of a crack to force ratio (Equation 12)

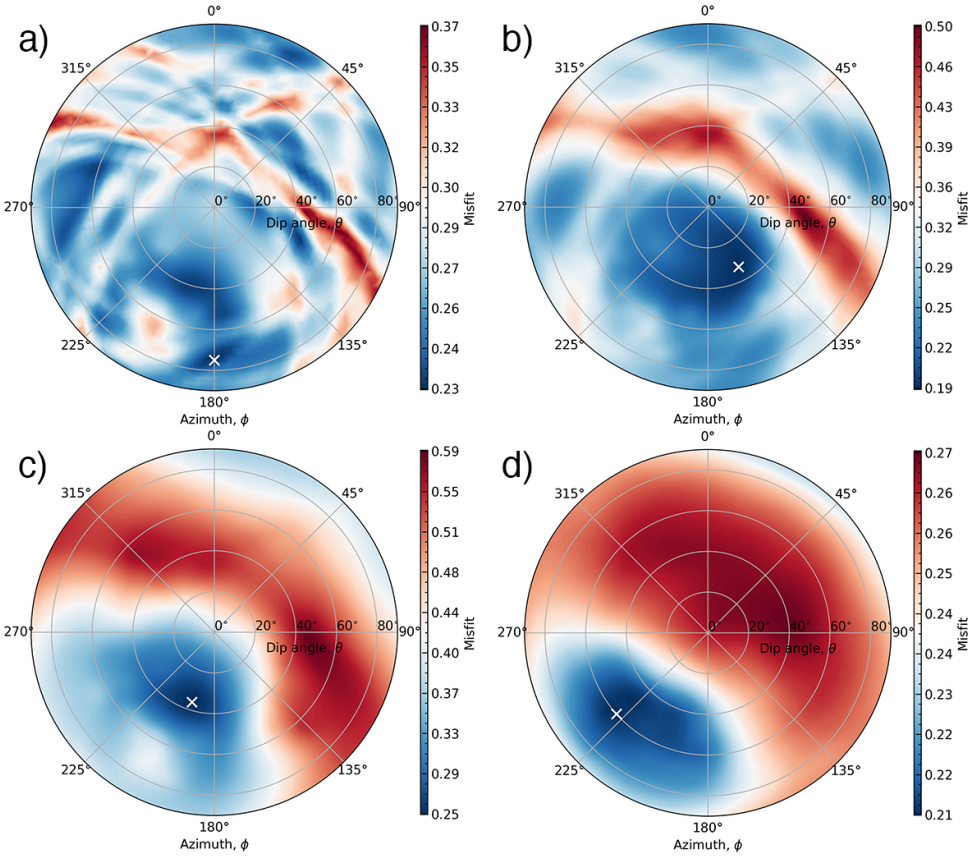

Fig. 14: Misfit distributions "stacked" for all selected DLP events for different source mechanisms. The misfits minima are shown with white crosses and have the following values: (a) Tensile crack $M_{L_1}^{stack} = 0.23$; (b) Cylindrical pipe $M_{L_1}^{stack} = 0.19$; (c) Single force $M_{L_1}^{stack} = 0.25$; (d) Combination of a horizontal tensile crack and a single force $M_{L_1}^{stack} = 0.21$

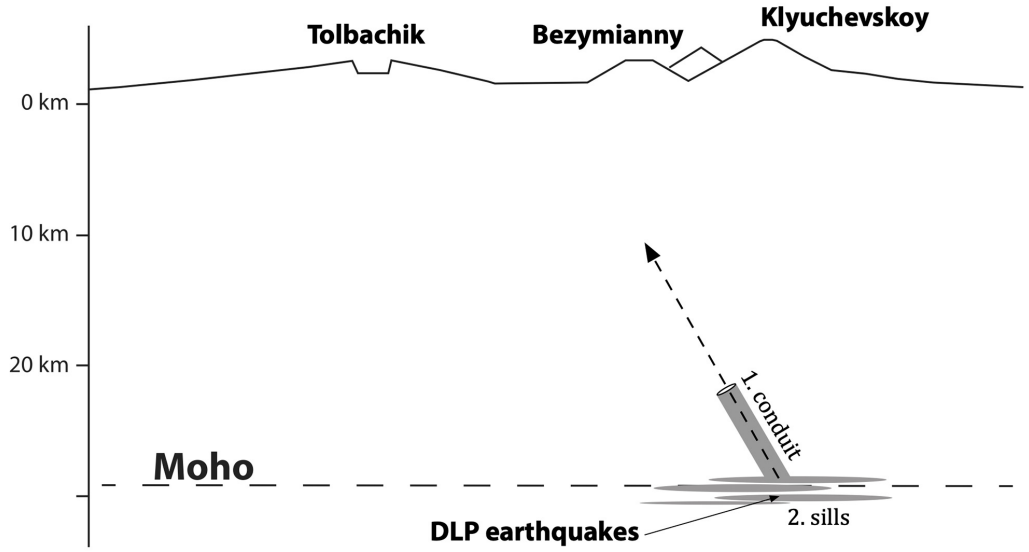

Fig. 15: Possible interpretation based on the obtained results schematically shown on a SSW-NNE oriented vertical cross-section indicating positions of three active KVG volcanoes.

No	Date	Time	Latitude	Longitude	Depth, km	M_L
1	2015-08-08	09:55:30	56.085	160.634	28.0	1.3
2	2015-08-09	23:24:57	56.077	160.628	27.4	1.4
3	2015-08-16	07:29:15	56.096	160.613	29.9	1.5
4	2015-08-16	12:14:57	56.066	160.611	28.4	1.3
5	2015-08-16	13:31:52	56.085	160.609	29.1	1.6
6	2015-08-20	12:23:54	56.084	160.616	26.1	1.6
7	2015-08-21	06:47:06	56.069	160.596	28.4	1.4
8	2015-08-25	10:36:26	56.083	160.582	27.2	1.4
9	2015-08-31	00:19:06	56.074	160.642	28.1	1.6
10	2015-09-02	02:09:31	56.051	160.634	29.5	1.4
11	2015-09-03	09:52:02	56.082	160.658	29.6	1.5
12	2015-09-04	16:25:07	56.100	160.595	27.0	1.4
13	2015-09-04	22:07:35	56.067	160.633	25.3	1.6
14	2015-09-10	23:28:12	56.062	160.652	27.5	1.5
15	2015-09-11	10:40:44	56.082	160.633	28.1	1.5
16	2015-09-14	14:47:30	56.072	160.625	27.5	1.6
17	2015-09-23	15:49:22	56.069	160.639	25.9	1.4
18	2015-09-29	07:15:15	56.078	160.623	28.4	1.3
19	2015-10-02	14:30:58	56.072	160.594	29.8	1.4
20	2015-10-02	17:44:59	56.070	160.586	31.2	1.4
21	2015-11-05	22:13:04	56.102	160.570	29.3	1.3
22	2015-11-23	03:18:38	56.084	160.608	27.6	1.8
23	2015-11-23	13:29:30	56.086	160.627	31.4	1.8

24	2015-11-26	06:28:15	56.078	160.610	29.2	1.5
25	2015-11-27	19:28:40	56.087	160.616	29.3	1.3
26	2015-11-27	22:05:23	56.079	160.613	24.7	1.3
27	2016-01-11	07:25:44	56.076	160.598	26.8	1.4
28	2016-05-21	11:40:28	56.088	160.619	29.4	1.7
29	2016-05-27	05:40:42	56.091	160.632	29.6	1.4

Table 1: List of selected deep long period earthquakes

		Fault		Crack		Pipe		Force		Crack + force	
Station	obs	calc	Δ	calc	Δ	calc	Δ	calc	Δ	calc	Δ
SV13	-0.15	0.71	0.86	-0.07	0.08	0.23	0.38	0.47	0.61	0.21	0.35
IR18	0.40	0.30	0.10	0.36	0.05	0.12	0.29	0.65	0.24	0.41	0.00
SV9	0.07	0.65	0.58	0.37	0.30	0.21	0.14	-0.15	0.23	0.10	0.03
IR17	-0.01	0.37	0.38	0.24	0.25	0.03	0.04	0.47	0.48	0.33	0.34
IR11	0.62	0.66	0.04	0.34	0.28	0.18	0.44	0.60	0.02	0.46	0.16
IR6	-0.20	0.63	0.83	-0.21	0.00	0.01	0.22	0.32	0.52	0.19	0.39
IR12	0.39	0.53	0.14	0.37	0.02	0.14	0.25	0.50	0.11	0.42	0.03
IR4	-0.10	0.62	0.72	0.37	0.47	0.12	0.22	-0.05	0.05	0.06	0.16
IR13	-0.01	0.50	0.50	0.31	0.32	0.20	0.20	0.45	0.46	0.39	0.39
SV7	-0.05	-0.01	0.04	0.13	0.18	0.23	0.28	0.17	0.22	0.21	0.26
IR3	0.28	0.40	0.12	0.33	0.04	0.13	0.16	-0.08	0.36	0.06	0.23
SV6	0.06	0.04	0.03	0.22	0.16	0.18	0.12	0.01	0.06	0.13	0.07
IR2	-0.21	0.24	0.45	0.27	0.48	0.13	0.34	0.02	0.24	0.11	0.32
OR13	0.65	0.73	0.08	0.35	0.30	0.21	0.44	0.65	0.01	0.48	0.17
IR1	0.16	0.18	0.03	0.16	0.00	0.15	0.01	0.13	0.03	0.16	0.01
SV4	0.10	0.60	0.51	0.37	0.27	-0.10	0.19	0.20	0.10	0.13	0.04
SV1	0.60	0.31	0.29	0.12	0.48	0.12	0.48	0.19	0.40	0.17	0.42
SV3	-0.09	0.38	0.47	0.16	0.25	0.05	0.15	0.23	0.32	0.16	0.26
OR20	0.09	0.47	0.39	-0.07	0.15	0.10	0.01	0.31	0.22	0.22	0.13

Table 2: Observed logarithms of amplitude ratios measured from seismograms and calculated values all considered source mechanisms (an example of a DLP on August 20, 2015 at 12:23:54

Appendix A. Theoretical radiation patterns of P- and S-waves

Radiation patterns appearing in Equations 1-6 can be expressed via the direction cosines γ (from a source to a receiver):

$$R_{i,j}^{FP} = \gamma_j \gamma_j \tag{A.1}$$

$$R_{i,j}^{FS} = \gamma_j \gamma_j - \delta_{i,j} \tag{A.2}$$

$$R_{i,j,k}^{MP} = \gamma_j \gamma_j \gamma_k \tag{A.3}$$

$$R_{i,j,k}^{MP} = (\gamma_j \gamma_j - \delta_{i,j}) \gamma_k \tag{A.4}$$

We use Cartesian coordinates with X axis directed toward the North, Y - toward the East, and Z - upward (Figure A.16). Direction cosines can be calculated with known direction from a source to a receiver expressed via two radial angles: azimuth $\varphi \in [0°, 360°]$ measured clockwise from the North and inclination $i_\xi \in [0°, 180°]$ measured from the upward vertical:

$$\begin{cases} \gamma_x = \sin i_\xi \cos \varphi \\ \gamma_y = \sin i_\xi \sin \varphi \\ \gamma_z = \cos i_\xi \end{cases} \tag{A.5}$$

Single force

The orientation of a single force described with two angles: azimuth $\phi_f \in [0°, 360°]$ measured clockwise from the East and dip angle $\theta_f \in [0°, 90°]$ mea-

sured from the upward vertical (Fig. 3a). Three components of a unity force can be expressed as projections on three axes:

$$\begin{cases} F_x = \sin\theta_f \cos\phi_f \\ F_y = \sin\theta_f \sin\phi_f \\ F_z = \cos\theta_f \end{cases} \tag{A.6}$$

Sources described by a moment tensor

Cylindrical pipe. Similar to a single force, its orientation is described by two angles: azimuth $\phi_p \in [0°, 360°]$ measured clockwise from the North and dip angle $\theta_p \in [0°, 90°]$ measured from the upward vertical (Fig. 3b). The corresponding components of the normalized moment rate tensor are (Kumagai, 2009):

$$\begin{aligned} M_{xx} &= M_0\,(1 + \cos^2\theta_p \cos^2\phi_p + \sin^2\phi_p) \\ M_{xy} &= -M_0\,\sin^2\theta_p \sin\phi_p \cos\phi_p \\ M_{xz} &= -M_0\,\sin\theta_p \cos\theta_p \cos\phi_p \\ M_{yy} &= M_0\,(1 + \cos^2\theta_p \sin^2\phi_p + \cos^2\phi_p) \\ M_{yz} &= M_0\,-\sin\theta_p \cos\theta_p \sin\phi_p \\ M_{zz} &= M_0\,(1 + \sin^2\theta_p) \end{aligned} \tag{A.7}$$

Shear slip is defined by three angles: ϕ_s, δ and λ

$$\begin{aligned}
M_{xx} &= -M_0 \left(\sin\delta\cos\lambda\sin 2\phi_s + \sin 2\delta\ \sin\lambda\ \sin^2\phi_s\right) \\
M_{xy} &= M_0 \left(\sin\delta\cos\lambda\cos 2\phi_s + \frac{1}{2}\sin 2\delta\sin\lambda\sin 2\phi_s\right) \\
M_{xz} &= -M_0 \left(\cos\delta\cos\lambda\cos\phi_s + \cos 2\delta\sin\lambda\sin\phi_s\right) \\
M_{yy} &= M_0 \left(\sin\delta\cos\lambda\sin 2\phi_s - \sin 2\delta\sin\lambda\cos^2\phi_s\right) \\
M_{yz} &= -M_0 \left(\cos\delta\cos\lambda\sin\phi_s - \cos 2\delta\sin\lambda\cos\phi_s\right) \\
M_{zz} &= M_0 \left(\sin 2\delta\sin\lambda\right)
\end{aligned} \tag{A.8}$$

Tensile crack is oriented by two angles: ϕ_c and θ_c

$$\begin{aligned}
M_{xx} &= M_0 \left(1 + 2\sin^2\theta_c\sin^2\phi_c\right) \\
M_{xy} &= -M_0 \left(\sin^2\theta_c\sin 2\phi_c\right) \\
M_{xz} &= M_0\ \sin 2\theta_c\sin\phi_c \\
M_{yy} &= M_0 \left(1 + 2\sin^2\theta_c\cos^2\phi_c\right) \\
M_{yz} &= -M_0 \left(\sin 2\theta_c\cos\phi_c\right) \\
M_{zz} &= M_0 \left(1 + 2\cos^2\theta_c\right)
\end{aligned}$$

Appendix B. Site amplification factors

Appendix B.1. Estimation of S-wave site amplification based on codas of seismograms

To estimate the S-wave site amplification we used the method based on coda of seismograms (Husker et al., 2010) that consist waves scattered at random heterogenities in the Earth. Because of the preferential P-to-S conversion druring the scattering of elastic waves, the seismic codas are dominated by

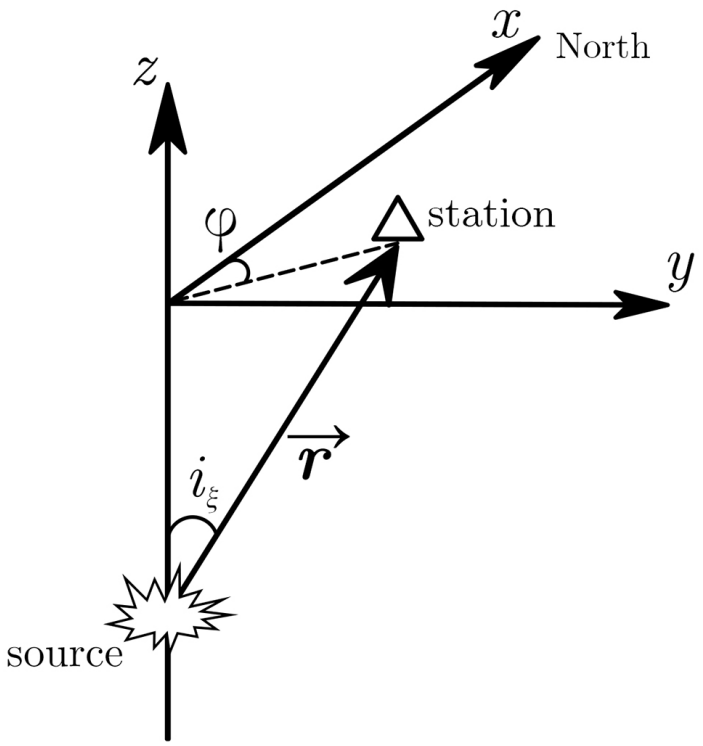

Fig. A.16: The coordinate system used in the study and definition of polar angles: azimuth $\varphi \in [0°, 360°]$ and inclination $i_\xi \in [0°, 180°]$

S-wave energy (e.g., Margerin et al., 2000; Shapiro et al., 2000). The coda envelope recorded at station i during event k can be expressed as (Aki and Chouet, 1975; Rautian and Khalturin, 1978):

$$A_{ik}(f,t) = S_k(f)\, R_i(f)\, I_i(f)\, G_i(f,t) \tag{B.1}$$

where f is the frequency, t is the lapse time, $S_k(f)$ is the source spectrum, $R_i(f)$ is the frequency-dependent site amplification, $I_i(f)$ is the instrument response, $G(f,t)$ is the term describing the wave propagation (Green's function). At times significantly greater than the arrival of direct S-waves, the energy of scattered seismic becomes uniformly distributed in the media and the term $G(f,t)$ becomes approximately equal at all stations. As a consequence, in the late coda, the ratio of the envelopes (computed after removing the instrument response) stabilized in time and becomes equal to the ratio of the site amplification factors:

$$\frac{A_{ik}(f,t)}{A_{jk}(f,t)} = \frac{R_i(f)}{R_j(f)} \tag{B.2}$$

We apply this equation to three-component envelopes computed from seismograms filtered between 1 and 4 Hz and smoothed with 50 s long moving window to estimate average amplification coefficients in this frequency range. An example for a pair of stations is shown in Figure B.18. The envelope ratios are computed within a window of 120 s length. Its starting time was chosen with visual inspection but it should be at least two times larger than the arrival of direct S-waves. For the example presented in Figure B.18 the starting and ending time were chosen as 110 s and 230 s correspondingly.

We select 7 sufficiently strong regional earthquakes (Table B.3) recorded

by the majority of the KISS network. Overall, we used 53 stations. By computing amplitude ratios for all possible pairs of stations and events, we have a set of measurements that we use to constrain average site amplifications in a least square sense (after taking logarithms of equation B.2). We also chose station OR13 located on a hard rock site well outside the volcanic edifices and sedimentary layers as a reference and all site amplification coefficients are computed relative to it.

Appendix B.2. Site amplifications of P-waves

P-wave amplification can be estimated from fist arriving P waves not contaminated by S-wave energy rapidly appearing in the p-wave coda because of the scattering. Telesemic P-waves can be used for this purpose at relatively low frequencies. In our spectral range of interest, 1-4 Hz, all teleseismic P waves recorded suring the KISS experiment were attenuated. Therefore, we decided to use nearly vertically incident P waves from relatively deep subduction earthquakes located approximately beneath the network. We found 4 such events listed in Table B.3 and shown in Figure B.17. The process of calculating P-wave amplification is illustrated in Figure B.19. For this example, a regional earthquake on October 16, 2015 at 06:38:23 was used. A significant source of uncertainty arises from the unknown radiation pattern of the used earthquakes. We can only assume, because of the nearly vertical incidence, the ray parameters do not differ strongly across the network and are close to the maxima of the P-wave radiation patterns expect from the subduction geometry.

Appendix B.3. Final results

During the study period we found 4 and 7 regional tectonic events to estimate averaged amplification coefficients for P- and S-waves. Their parameters are presented in Table B.3 and the epicenters are shown in Fig. B.17. The site amplification coefficients were estimated stations used for the source mechanism inversion for both P- and S-waves are shown in Table B.4.

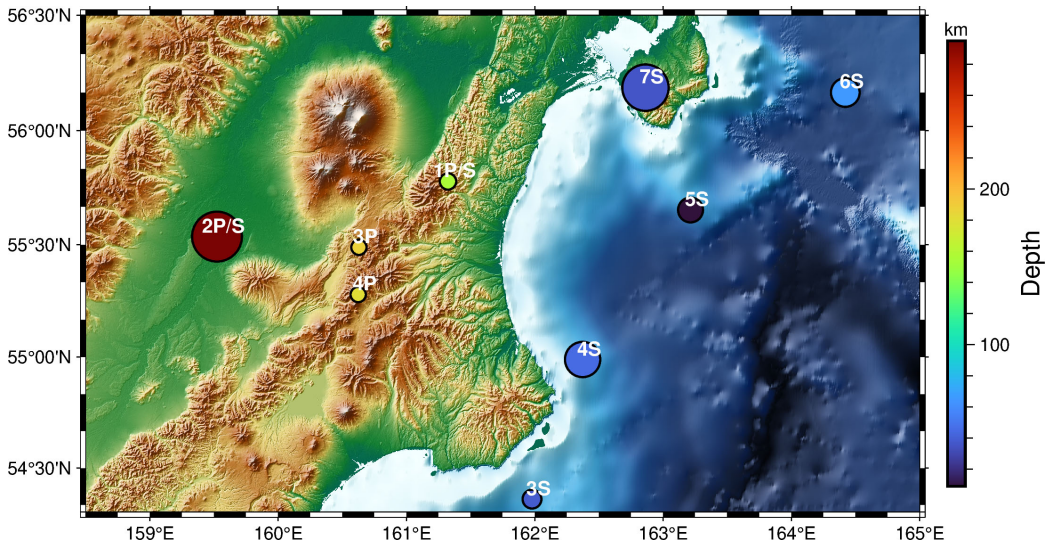

Fig. B.17: Map of the epicenters of the earthquakes used for measuring amplifications of P- and S-waves, their codes correspond to the codes in Table B.3. The circle size represents the corresponding event magnitude.

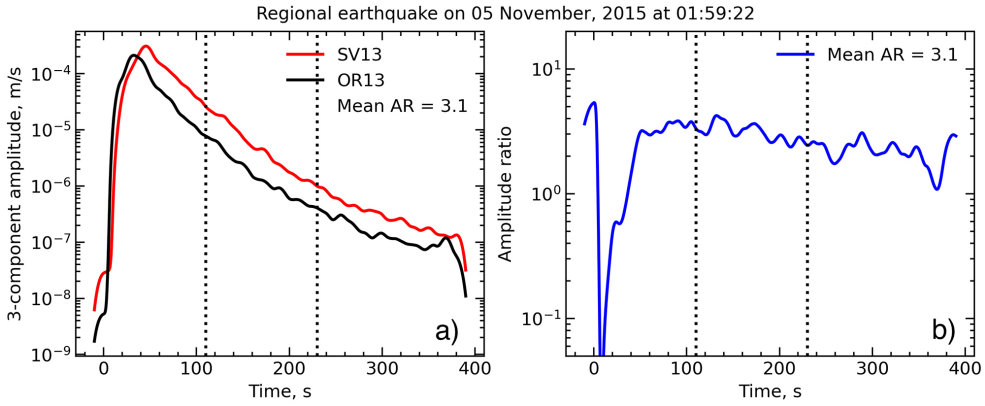

Fig. B.18: Example of measuring a relative amplification of S-waves between two stations from the coda of seismograms (a) Smoothed three-component envelopes. (b) Amplitude ratios between two stations. Dotted lines show the beginning and the end of 120 s long coda window.

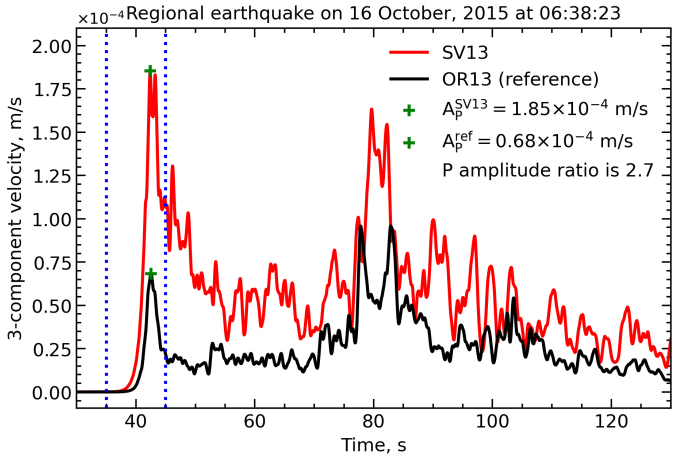

Fig. B.19: Measuring P-wave site amplification at station OR13, green crosses show the defined P-wave amplitudes

	P-waves	S-waves
1	2015-11-02 20:02:48 (M = 4.3, z = 156 km)	
2	2015-10-16 06:38:23 (M = 5.9, z = 295 km)	
3	2015-11-18 22:37:27 (M = 4.2, z = 187 km)	2015-11-29 23:45:55 (M = 4.5, z = 38 km)
4	2016-02-08 04:25:03 (M = 4.2, z = 180 km)	2016-02-01 22:47:51 (M = 5.4, z = 45 km)
5		2015-09-29 04:33:27 (M = 4.9, z = 9 km)
6		2015-08-24 11:50:55 (M = 5.1, z = 65 km)
7		2015-11-05 01:59:22 (M = 5.8, z = 36 km)

Table B.3: Regional earthquakes used for estimation of amplification coefficients.

	P-waves amplification	S-waves amplification
IR1	1.50 ± 0.81	1.98 ± 0.39
IR11	2.27 ± 0.74	4.51 ± 1.25
IR12	2.05 ± 0.82	4.20 ± 1.12
IR13	2.20 ± 0.87	3.91 ± 0.75
IR17	0.91 ± 0.66	1.40 ± 0.27
IR18	0.60 ± 0.48	1.61 ± 0.37
IR2	1.20 ± 0.53	3.33 ± 0.91
IR3	2.16 ± 2.34	3.15 ± 0.82
IR4	1.01 ± 0.48	2.62 ± 0.65
IR6	0.58 ± 0.58	1.35 ± 0.31
OR13	1.00 ± 0.00	1.00 ± 0.00
OR20	1.93 ± 0.49	3.44 ± 0.62
SV1	1.35 ± 0.69	1.76 ± 0.33
SV13	1.47 ± 0.83	3.13 ± 0.61
SV3	0.90 ± 0.39	2.30 ± 0.60
SV4	1.58 ± 2.06	3.64 ± 1.04
SV6	0.71 ± 0.47	1.42 ± 0.27
SV7	1.56 ± 0.89	3.22 ± 0.68
SV9	1.02 ± 0.82	1.07 ± 0.22

Table B.4: Average amplification coefficients and their standard deviations.

Appendix C. Discretization of the mechanism orientation space for the grid search

In order to calculate the misfit function a grid of possible source orientations should be defined.

Two parameters case

For source mechanisms whose orientation depends on two angles (a single force, a tensile crack, a cylindrical pipe) the grid of parameters is compiled by dividing a disk or a hemisphere into cells of equal area. Firstly, the range of values of the dip angle $\theta \in [0°, 90°]$ was uniformly discretized into N_θ points with a step $\Delta\theta$. At the next step the same parameter $\Delta\theta$ was used to define a number of intervals N_ϕ making up the outer circle, i.e. the one that corresponds to $\theta = 90°$:

$$N_\phi^{outer} = \frac{360°}{\Delta\theta} \tag{C.1}$$

After all, the amount of points in every circle of θ_i was defined into two steps. Equation C.2 allowed to calculate an aspect ratio a_i for a circle corresponding to θ_i.

$$a_i = \sin\,\theta_i \tag{C.2}$$

Then, the obtained aspect ratio was used for calculating a number of points in a circle corresponding to θ_i:

$$N_\phi^i = a_i\, N_\phi^{outer} \tag{C.3}$$

In this work $\Delta\theta$ was taken as 3° what provides $N_\theta = 31$ and $N_\phi^{outer} = 70$ (Figure C.20). This configuration allowed to perform the grid search thorough enough but not computationally expensive at the same time.

Three parameters case

The classic shear slip model requires three angles to orient a source in space. Thus, besides strike ϕ_s and dip δ the grid of parameters becomes three dimensional due to rake angle $\lambda \in [0^\circ, 180^\circ]$. The range of possible rake values was discretized with a step of 3° as well. Then, the combined mechanism included an additional parameter responsible for the contribution of one or another source: a force or a horizontal crack. This ratio can be expressed as:

$$r = \frac{A_{crack}}{A_{crack} + A_{force}} \tag{C.4}$$

If $r \to 1$, a horizontal crack is dominating, while when $r \to 0$ the dominating mechanism is a single force in both cases. Parameter r lies in the range $[1/6, 5/6]$ or, in other words, ratio $A_{crack} : A_{force}$ varies from 1:5 to 5:1.

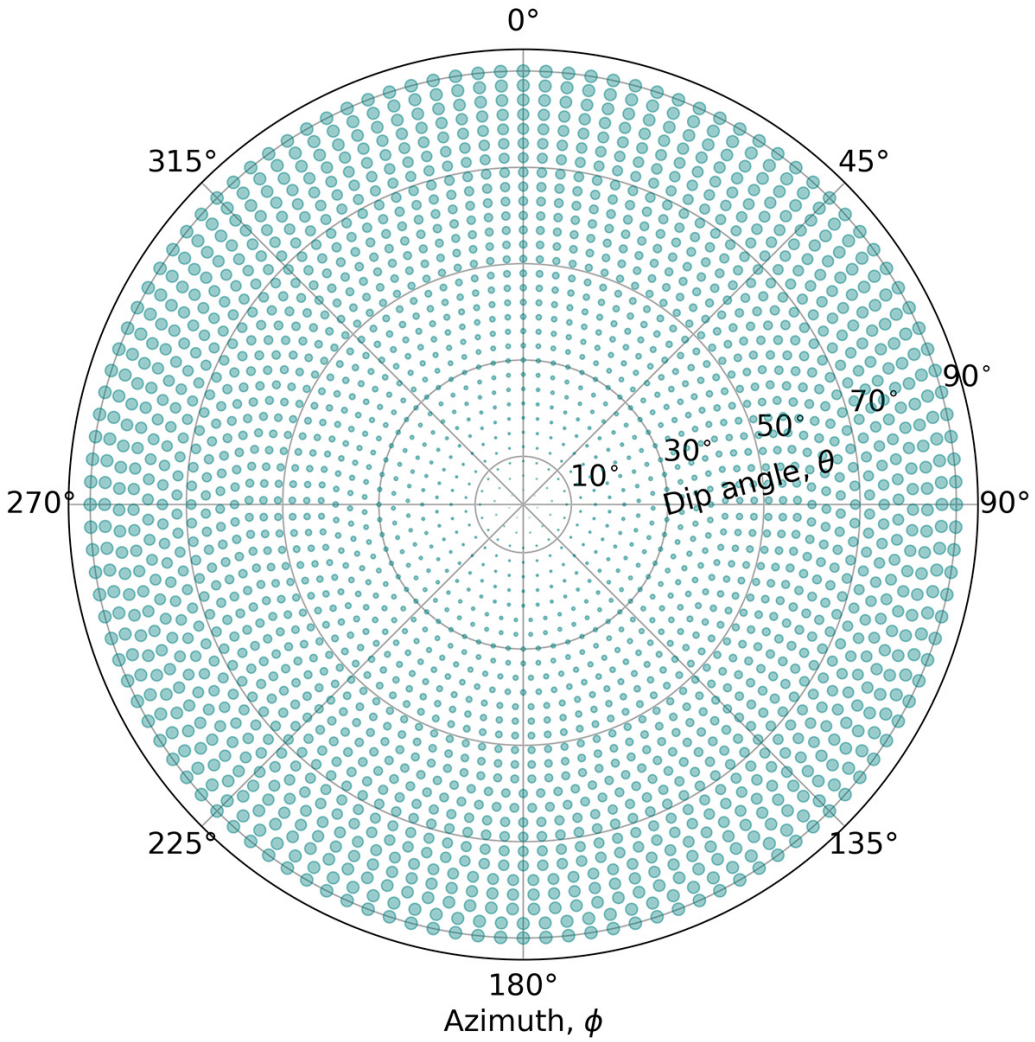

Fig. C.20: Two dimensional grid in polar coordinates

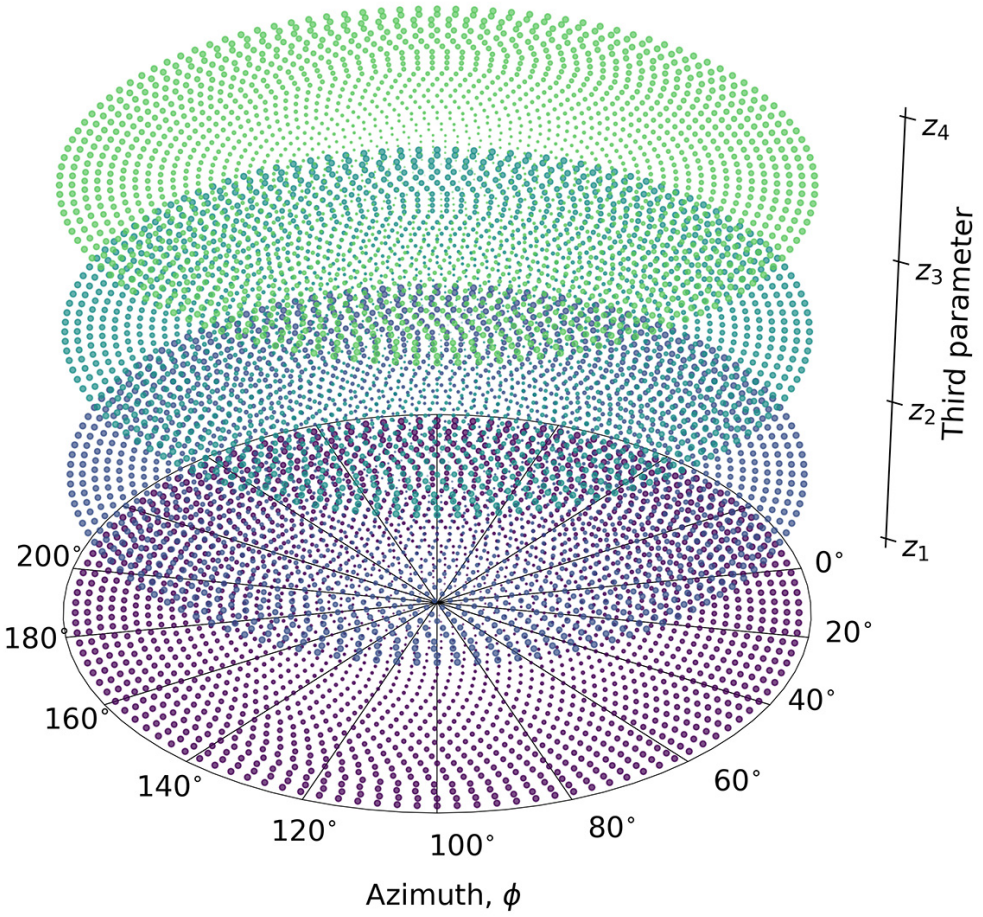

Fig. C.21: Three dimensional grid in polar coordinates. Vertical axis is obtained by discretizing a third parameter: either a rake angle λ or a ratio r which defines a dominating mechanism a combined source

References

Aki, K., Chouet, B., 1975. Origin of coda waves: source, attenuation, and scattering effects. J. Geophys. Res. 80, 3322–3342. doi:10.1016/S0031-8914(53)80099-6.

Aki, K., Richards, P.G., 1980. Quantitative Seismology: Theory and Methods. volume 842. San Francisco, CA: Freeman. doi:10.1002/gj.3350160110.

Annen, C., Bundy, J.D., Sparks, R.S.J., 2005. The Genesis of Intermediate and Silicic Magmas in Deep Crustal Hot Zones. Journal of Petrology 47, 505–539. doi:10.1093/petrology/egi084.

Aso, N., Ide, S., 2014. Focal mechanisms of deep low-frequency earthquakes in eastern shimane in western japan. Journal of Geophysical Research: Solid Earth 119, 364–377. doi:https://doi.org/10.1002/2013JB010681.

Aso, N., Ohta, K., Ide, S., 2013. Tectonic, volcanic, and semi-volcanic deep low-frequency earthquakes in western japan. Tectonophysics 600, 27–40. doi:https://doi.org/10.1016/j.tecto.2012.12.015.

Aso, N., Tsai, V.C., 2014. Cooling magma model for deep volcanic long-period earthquakes. J. Geophys. Res. Solid Earth 119, 8442–8456. doi:10.1002/2014JB011180.

Bean, C.J., De Barros, L., Lokmer, I., Métaxian, J.P., O'Brien, G., Murphy, S., 2014. Long-period seismicity in the shallow volcanic edifice formed from slow-rupture earthquakes. Nature Geoscience 7, 71–75. doi:10.1038/ngeo2027.

667 Campillo, M., Plantet, J., 1991. Frequency dependence and spatial distri-
668 bution of seismic attenuation in france: experimental results and possible
669 interpretations. Physics of the Earth and Planetary Interiors 67, 48–64.
670 doi:https://doi.org/10.1016/0031-9201(91)90059-Q.

671 Chouet, B., 1996. Long-period volcano seismicity: its source and use in
672 eruption forecasting. Nature 380, 309–316. doi:10.1038/380309a0.

673 Chouet, B., 2003. Volcano seismology. Pure and applied geophysics 160,
674 739–788.

675 Chouet, B., Dawson, P., Arciniega-Ceballos, A., 2005. Source mechanism
676 of vulcanian degassing at popocatépetl volcano, mexico, determined from
677 waveform inversions of very long period signals. Journal of Geophysical Re-
678 search: Solid Earth 110. doi:https://doi.org/10.1029/2004JB003524.

679 Chouet, B., Dawson, P., Ohminato, T., Martini, M., Saccorotti, G., Giudi-
680 cepietro, F., De Luca, G., Milana, G., Scarpa, R., 2003. Source mecha-
681 nisms of explosions at stromboli volcano, italy, determined from moment-
682 tensor inversions of very-long-period data. Journal of Geophysical Re-
683 search: Solid Earth 108, ESE 7–1–ESE 7–25. doi:https://doi.org/10.
684 1029/2002JB001919.

685 Chouet, B., Matoza, R.S., 2013. A multi-decadal view of seismic methods
686 for detecting precursors of magma movement and eruption. J. Volcanol.
687 Geotherm. Res. 252, 109–175. doi:10.1016/j.jvolgeores.2012.11.013.

688 Coppola, D., Laiolo, M., Massimetti, F., Hainzl, S., Shevchenko, A.V., Ma-
689 nia, R., Shapiro, N.M., Walter, T.R., 2021. Thermal remote sensing reveals

communication between volcanoes of the klyuchevskoy volcanic group. Scientific Reports 11, 13090. doi:10.1038/s41598-021-92542-z.

Dorendorf, F., Wiechert, U., Wörner, G., 2000. Hydrated sub-arc mantle: a source for the kluchevskoy volcano, kamchatka/russia. Earth and Planetary Science Letters 175, 69–86. doi:https://doi.org/10.1016/S0012-821X(99)00288-5.

Droznin, D., Shapiro, N., Droznina, S.Y., Senyukov, S., Chebrov, V., Gordeev, E., 2015. Detecting and locating volcanic tremors on the Klyuchevskoy group of volcanoes (Kamchatka) based on correlations of continuous seismic records. Geophysical Journal International 203, 1001–1010. doi:10.1093/gji/ggv342.

Droznin, D.V., Droznina, S.Y., 2011. Interactive dimas program for processing seismic signals. Seismic Instruments 47, 215.

Fedotov, S.A., Zharinov, N.A., Gontovaya, L.I., 2010. The magmatic system of the klyuchevskaya group of volcanoes inferred from data on its eruptions, earthquakes, deformation, and deep structure. J. Volcanol. Geotherm. Res. 4, 1–33. doi:10.1134/S074204631001001X.

Frank, W.B., Shapiro, N.M., Gusev, A.A., 2018. Progressive reactivation of the volcanic plumbing system beneath tolbachik volcano (kamchatka, russia) revealed by long-period seismicity. Earth and Planetary Science Letters 493, 47–56. doi:https://doi.org/10.1016/j.epsl.2018.04.018.

Galina, N.A., Shapiro, N.M., Droznin, D.V., Droznina, S.Y., Senyukov, S.L., Chebrov, D.V., 2020. Recurrence of deep long-period earthquakes beneath

the klyuchevskoi volcano group, kamchatka. Izvestiya, Physics of the Solid Earth 56, 749–761. doi:10.1134/S1069351320060026.

Gorelchik, V.I., Garbuzova, V.T., Storcheus, A.V., 2004. Deep-seated volcanic processes beneath klyuchevskoi volcano as inferred from seismological data. Journal of Volcanology and Seismology 6, 21–34.

Green, R.G., Sens-Schönfelder, C., Shapiro, N., Koulakov, I., Tilmann, F., Dreiling, J., Luehr, B., Jakovlev, A., Abkadyrov, I., Droznin, D., Gordeev, E., 2020. Magmatic and sedimentary structure beneath the klyuchevskoy volcanic group, kamchatka, from ambient noise tomography. Journal of Geophysical Research: Solid Earth 125, e2019JB018900. doi:https://doi.org/10.1029/2019JB018900.

Hardebeck, J.L., Shearer, P.M., 2003. Using S/P Amplitude Ratios to Constrain the Focal Mechanisms of Small Earthquakes. Bulletin of the Seismological Society of America 93, 2434–2444. doi:10.1785/0120020236.

Hasegawa, A., Yamamoto, A., 1994. Deep, low-frequency microearthquakes in or around seismic low-velocity zones beneath active volcanoes in northeastern japan. Tectonophysics 233, 233–252. doi:https://doi.org/10.1016/0040-1951(94)90243-7.

Hensch, M., Dahm, T., Ritter, J., Heimann, S., Schmidt, B., Stange, S., Lehmann, K., 2019. Deep low-frequency earthquakes reveal ongoing magmatic recharge beneath Laacher See Volcano (Eifel, Germany). Geophysical Journal International 216, 2025–2036. doi:10.1093/gji/ggy532.

735 Husker, A., Peyrat, S., Shapiro, N., Kostoglodov, V., 2010. Automatic non-
736 volcanic tremor detection in the mexican subduction zone. Geofis. Int. 49,
737 17–25.

738 Ikegaya, T., Yamamoto, M., 2021. Spatio-temporal characteristics and focal
739 mechanisms of deep low-frequency earthquakes beneath the zao volcano,
740 northeastern japan. Journal of Volcanology and Geothermal Research 417,
741 107321. doi:https://doi.org/10.1016/j.jvolgeores.2021.107321.

742 Ivanov, A., Koulakov, I., West, M., Jakovlev, A., Gordeev, E., Senyukov,
743 S., Chebrov, V., 2016. Magma source beneath the bezymianny volcano
744 and its interconnection with klyuchevskoy inferred from local earthquake
745 seismic tomography. J. Volcanol. Geotherm. Res 323, 62–71. doi:10.1016/
746 j.jvolgeores.2016.04.010.

747 Journeau, C., Shapiro, N. M.and Seydoux, L., Soubestre, J., Koulakov, I.Y.,
748 Jakovlev, A.V., Abkadyrov, I., Gordeev, E.I., Chebrov, D.V., Droznin,
749 D.V., Sens-Schönfelder, C., Luehr, B.G., Tong, F., Farge, G., Jaupart,
750 C., 2022. Seismic tremor reveals active trans-crustal magmatic system be-
751 neath kamchatka volcanoes. Sci. Adv. 8, eabj1571. doi:10.1126/sciadv.
752 abj1571.

753 Koulakov, I., Abkadyrov, I., Al Arifi, N., Deev, E., Droznina, S., Gordeev,
754 E.I., Jakovlev, A., El Khrepy, S., Kulakov, R.I., Kugaenko, Y., Nov-
755 gorodova, A., Senyukov, S., Shapiro, N., Stupina, T., West, M., 2017.
756 Three different types of plumbing system beneath the neighboring active
757 volcanoes of tolbachik, bezymianny, and klyuchevskoy in kamchatka. Jour-

nal of Geophysical Research: Solid Earth 122, 3852–3874. doi:https://doi.org/10.1002/2017JB014082.

Koulakov, I., Plechov, P., Mania, R., Walter, T.R., Smirnov, S.Z., Abkadyrov, I., Jakovlev, A., Davydova, V., Senyukov, S., Bushenkova, N., Novgorodova, A., Stupina, T., Droznina, S.Y., 2021. Anatomy of the bezymianny volcano merely before an explosive eruption on 20.12.2017. Scientific Reports 11, 1758. doi:10.1038/s41598-021-81498-9.

Koulakov, I., Shapiro, N.M., Sens-Schönfelder, C., Luehr, B.G., Gordeev, E.I., Jakovlev, A., Abkadyrov, I., Chebrov, D.V., Bushenkova, N., Droznina, S.Y., Senyukov, S.L., Novgorodova, A., Stupina, T., 2020. Mantle and crustal sources of magmatic activity of klyuchevskoy and surrounding volcanoes in kamchatka inferred from earthquake tomography. Journal of Geophysical Research: Solid Earth 125, e2020JB020097. doi:10.1029/2020JB020097.

Kumagai, H., 2009. Volcano seismic signals, source quantification of, in: Meyers, R.A. (Ed.), Encyclopedia of Complexity and Systems Science. Springer New York, New York, NY, pp. 9899–9932. doi:10.1007/978-0-387-30440-3_583.

Kurihara, R., Obara, K., 2021. Spatiotemporal characteristics of relocated deep low-frequency earthquakes beneath 52 volcanic regions in japan over an analysis period of 14 years and 9 months. J. Geophys. Res. Solid Earth 126, e2021JB022173. doi:10.1029/2021JB022173.

Kurihara, R., Obara, K., Takeo, A., Tanaka, Y., 2019. Deep low-frequency

earthquakes associated with the eruptions of shinmoe-dake in kirishimavolcanoes. J. Geophys. Res. Solid Earth 124, 13079–13095. doi:10.1029/2019JB018032.

Levin, V., Droznina, S.Y., Gavrilenko, M., Carr, M.J., Senyukov, S.L., 2014. Seismically active subcrustal magma source of the klyuchevskoy volcano in kamchatka, russia. Geol. 42, 983–986. doi:10.1130/G35972.1.

Levin, V., Shapiro, N., Park, J., Ritzwoller, M., 2002. Seismic evidence for catastrophic slab loss beneath kamchatka. Nature 418, 763–767. doi:10.1038/nature00973.

Margerin, L., Campillo, M., Van Tiggelen, B., 2000. Monte carlo simulation of multiple scattering of elastic waves. Journal of Geophysical Research: Solid Earth 105, 7873–7892. doi:https://doi.org/10.1029/1999JB900359.

Matoza, R.S., Roman, D.C., 2022. One hundred years of advances in volcano seismology and acoustics. Bulletin of Volcanology 84, 86. doi:10.1007/s00445-022-01586-0.

McNutt, S.R., Roman, D.C., 2015. Chapter 59 - volcanic seismicity, in: Sigurdsson, H. (Ed.), The Encyclopedia of Volcanoes (Second Edition). second edition ed.. Academic Press, Amsterdam, pp. 1011–1034. doi:https://doi.org/10.1016/B978-0-12-385938-9.00059-6.

Melnik, O., Lyakhovsky, V., Shapiro, N.M., Galina, N., Bergal-Kuvikas, O., 2020. Deep long period volcanic earthquakes generated by degassing of

volatile-rich basaltic magmas. Nature Communications 11, 3918. doi:10.1038/s41467-020-17759-4.

Melnik, O.E., Utkin, I.S., Bindeman., I.N., 2022. Magma chamber formation by dike accretion and crustal melting: 2d thermal model with emphasis on zircon record. Authorea doi:10.1002/essoar.10505594.1.

Nakamichi, H., Hamaguchi, H., Tanaka, S., Ueki, S., Nishimura, T., Hasegawa, A., 2003. Source mechanisms of deep and intermediate-depth low-frequency earthquakes beneath iwate volcano, northeastern japan. Geophysical Journal International 154, 811–828. doi:https://doi.org/10.1046/j.1365-246X.2003.01991.x.

Nichols, M., Malone, S., Moran, S., Thelen, W., Vidale, J., 2011. Deep long-period earthquakes beneath washington and oregon volcanoes. J. Volcanol. Geotherm. Res. 200, 116–128. doi:10.1016/j.jvolgeores.2010.12.005.

Nishimura, T., Iguchi, M., 2011. Volcanic Earthquakes and Tremor in Japan. Kyoto University Press.

Niu, X., Zhao, D., Li, J., 2017. Precise relocation of low-frequency earthquakes in northeast japan: new insight into arc magma and fluids. Geophys. J. Int. 212, 1183–1200. doi:10.1093/gji/ggx445.

Ohmi, S., Obara, K., 2002. Deep low-frequency earthquakes beneath the focal region of the mw 6.7 2000 western tottori earthquake. Geophys. Res. Lett. 29, 54–1–54–4. doi:10.1029/2001GL014469.

Ohminato, T., Chouet, B.A., Dawson, P., Kedar, S., 1998. Waveform inversion of very long period impulsive signals associated with magmatic

injection beneath kilauea volcano, hawaii. Journal of Geophysical Research: Solid Earth 103, 23839–23862. doi:https://doi.org/10.1029/98JB01122.

Power, J., Stihler, S., White, R., Moran, S., 2004. Observations of deep long-period (dlp) seismic events beneath aleutian arc volcanoes; 1989–2002. J. Volcanol. Geotherm. Res 138, 243–266. doi:10.1016/j.jvolgeores.2004.07.005.

Rautian, T.G., Khalturin, V.I., 1978. The use of the coda for determination of the earthquake source spectrum. Bull. Seismol. Soc. Am. 68, 923–948. doi:10.1785/BSSA0680040923.

Roman, D.C., Cashman, K.V., 2006. The origin of volcano-tectonic earthquake swarms. Geology 34, 457–460. doi:10.1130/G22269.1.

Rubin, A.M., 1995. Propagation of magma-filled cracks. Annual Review of Earth and Planetary Sciences 23, 287–336. doi:10.1146/annurev.ea.23.050195.001443.

Sato, H., 1984. Attenuation and envelope formation of three-component seismograms of small local earthquakes in randomly inhomogeneous lithosphere. Journal of Geophysical Research: Solid Earth 89, 1221–1241. doi:https://doi.org/10.1029/JB089iB02p01221.

Senyukov, S., Droznin, D., Droznina, S., Shapiro, N., Nuzhdina, I., Kozhevnikova, T., Sobolevskaya, O., Nazarova, Z., Dolzhikova, A., Toloknova, S., Karpenko, E., 2021. Catalog of earthquakes from the data of the kiss seismic network in 2015-2016, in: Proceedings of the

Eighth All-Russian Scientific and Technical Conference: Problems of integrated geophysical monitoring of seismically active regions, Petropavlovsk-Kamchatsky, Russia. pp. 216–2020.

Senyukov, S.L., 2013. Monitoring and prediction of volcanic activity in kamchatka from seismological data: 2000–2010. Journal of Volcanology and Seismology 7, 86–97. doi:10.1134/S0742046313010077.

Senyukov, S.L., Droznina, S.Y., Nuzhdina, I.N., Garbuzova, V.T., Kozhevnikova, T.Y., 2009. Studies in the activity of klyuchevskoi volcano by remote sensing techniques between january 1, 2001 and july 31, 2005. Journal of Volcanology and Seismology 3, 191–199. doi:10.1134/S0742046309030051.

Shapiro, N.M., Campillo, M., Kaminski, E., Vilotte, J.P., Jaupart, C., 2018. Low-frequency earthquakes and pore pressure transients in subduction zones. Geophysical Research Letters 45, 11,083–11,094. doi:https://doi.org/10.1029/2018GL079893.

Shapiro, N.M., Campillo, M., Margerin, L., Singh, S.K., Kostoglodov, V., Pacheco, J., 2000. The Energy Partitioning and the Diffusive Character of the Seismic Coda. Bulletin of the Seismological Society of America 90, 655–665. doi:10.1785/0119990021.

Shapiro, N.M., Droznin, D.V., Droznina, S.Y., Senyukov, S.L., Gusev, A.A., Gordeev, E.I., 2017a. Deep and shallow long-period volcanic seismicity linked by fluid-pressure transfer. Nat. Geosci. 10, 442–445. doi:10.1038/ngeo2952.

Shapiro, N.M., Sens-Schönfelder, C., Lühr, B.G., Weber, M., Abkadyrov, I., Gordeev, E.I., Kulakov, I.Y., Jakovlev, A., Kugaenko, Y.A., Saltykov, V.A., 2017b. Understanding kamchatka's extraordinary volcano cluster. Eos 98. doi:10.1029/2017EO071351.

Soubestre, J., Seydoux, L., Shapiro, N.M., de Rosny, J., Droznin, D.V., Droznina, S.Y., Senyukov, S.L., Gordeev, E.I., 2019. Depth migration of seismovolcanic tremor sources below the klyuchevskoy volcanic group (kamchatka) determined from a network-based analysis. Geophysical Research Letters 46, 8018–8030. doi:https://doi.org/10.1029/2019GL083465.

Soubestre, J., Shapiro, N.M., Seydoux, L., de Rosny, J., Droznin, D.V., Droznina, S.Y., Senyukov, S.L., Gordeev, E.I., 2018. Network-based detection and classification of seismovolcanic tremors: Example from the klyuchevskoy volcanic group in kamchatka. Journal of Geophysical Research: Solid Earth 123, 564–582. doi:https://doi.org/10.1002/2017JB014726.

Sparks, R., 2003. Forecasting volcanic eruptions. Earth and Planetary Science Letters 210, 1–15. doi:https://doi.org/10.1016/S0012-821X(03)00124-9.

Takei, Y., Kumazawa, M., 1994. Why have the single force and torque been excluded from seismic source models? Geophysical Journal International 118, 20–30. doi:10.1111/j.1365-246X.1994.tb04672.x.

Thelen, W., West, M., Senyukov, S., 2010. Seismic characterization of the

fall 2007 eruptive sequence at bezymianny volcano, russia. Journal of Volcanology and Geothermal Research 194, 201–213. doi:https://doi.org/10.1016/j.jvolgeores.2010.05.010.

Thelen, W.A., Matoza, R.S., Hotovec-Ellis, A.J., 2022. Trends in volcano seismology: 2010 to 2020 and beyond. Bulletin of Volcanology 84, 26. doi:10.1007/s00445-022-01530-2.

Ukawa, M., Ohtake, M., 1987. A monochromatic earthquake suggesting deep-seated magmatic activity beneath the izu-ooshima volcano, japan. J. Geophys. Res. Solid Earth 92, 12649–12663. doi:10.1029/JB092iB12p12649.

Wech, A.G., Thelen, W.A., Thomas, A.M., 2020. Deep long-period earthquakes generated by second boiling beneath mauna kea volcano. Science 368, 775–779. doi:10.1126/science.aba4798.

White, R.A., Newhall, C.G., Punongbayan, R.S., 1996. Precursory deep long-period earthquakes at mount pinatubo: Spatio-temporal link to a basalt trigger. Fire and mud: Eruptions and lahars of Mount Pinatubo, Philippines , 307–328.

Yogodzinski, G., Lees, J., Churikova, T., Dorendorf, F., Wöerner, G., Volynets, O., 2001. Geochemical evidence for the melting of subducting oceanic lithosphere at plate edges. Nature 409, 500–504. doi:10.1038/35054039.

Yoshimoto, K., Sato, H., Ohtake, M., 1993. Frequency-dependent attenuation of P and S waves in the Kanto area, Japan, based on the coda-

normalization method. Geophysical Journal International 114, 165–174. doi:10.1111/j.1365-246X.1993.tb01476.x.

Yukutake, Y., Abe, Y., Doke, R., 2019. Deep low-frequency earthquakes beneath the hakone volcano, central japan, and their relation to volcanic activity. Geophysical Research Letters 46, 11035–11043. doi:https://doi.org/10.1029/2019GL084357.

Zobin, V.M., 2011. Introduction to Volcanic Seismology. Elsevier.